# The Gibbs free energy landscape based on liver metabolome revealed thermodynamic robustness against fasting and obesity

Takumi Abekawa[1], Satoshi Ohno[1,2,3,*], Akiyoshi Hirayama[4], Tomoyoshi Soga[4,5], Shinya Kuroda[1,2,*]

[1]Department of Biological Sciences, Graduate School of Science, The University of Tokyo, 7-3-1 Hongo, Bunkyo-ku, Tokyo 113-0033, Japan.

[2]Molecular Genetics Research Laboratory, Graduate School of Science, The University of Tokyo, 7-3-1 Hongo, Bunkyo-ku, Tokyo, Japan.

[3]Department of AI Systems Medicine, M&D Data Science Center, Institute of Integrated Research, Institute of Science Tokyo, 1-5-45 Yushima, Bunkyo-ku, Tokyo 113-8510, Japan.

[4]Institute for Advanced Biosciences, Keio University, 246-2 Mizukami, Kakuganji, Tsuruoka, Yamagata 997-0052, Japan

[5]Human Biology-Microbiome-Quantum Research Center (WPI-Bio2Q), Keio University, Tsuruoka, Yamagata 997-0052, Japan

[*]Correspondence to: s-ohno.dsc@tmd.ac.jp (S.O.)

[*]Correspondence to: skuroda@bs.s.u-tokyo.ac.jp (S.K.)

**Abstract**

Mammalian liver metabolism undergoes a substantial shift during fasting. Thermodynamic principles impose fundamental constraints on metabolism, and the Gibbs free energy change of reaction ($\Delta_r G'$) indicates the reaction's direction and distance from equilibrium. However, $\Delta_r G'$ landscapes in intact mammalian organs remain largely uncharacterized. Here, we mapped $\Delta_r G'$ profile of glucose metabolism in mouse liver during fasting, using experimentally measured absolute metabolite concentrations and a newly developed computational method, GLEAM. We found that despite large metabolite fluctuations during fasting, the corresponding $\Delta_r G'$s remained robust, even for reactions reversing the direction between glycolysis and gluconeogenesis. A remarkable thermodynamic robustness is found in maintaining potential candidates of rate-limiting steps during fasting. This robustness is achieved by expending substantial costs for enzyme expressions, contributing to efficient switching from glycolysis to gluconeogenesis. Furthermore, obese mouse liver also showed thermodynamic robustness despite obesity-induced metabolic disruption. Our framework provided a novel thermodynamic perspective on intact organ metabolism, demonstrating that the liver robustly maintains thermodynamic characteristics favorable for metabolic control by buffering metabolite concentration differences.

37 **Glossary**

| Metabolite abbreviations | Metabolite names |
|---|---|
| G6P | Glucose 6-phosphate |
| F6P | Fructose 6-phosphate |
| F1,6BP | Fructose 1,6-bisphosphate |
| ADP | ADP |
| ATP | ATP |
| DHAP | Glycerone phosphate |
| GAP | Glyceraldehyde 3-phosphate |
| NAD | $NAD^+$ |
| NADH | NADH |
| Pi | Orthophosphate |
| 3PG | 3-Phospho-D-glycerate |
| 2PG | 2-Phospho-D-glycerate |
| PEP | Phosphoenolpyruvate |
| H2O | H2O |
| G1P | Glucose 1-phosphate |
| G3P | sn-Glycerol 3-phosphate |
| Pyr | Pyruvate |
| CoA | Coenzyme A |
| CO2 | CO2 |
| AcCoA | Acetyl-CoA |

| | |
|---|---|
| OAA | Oxaloacetate |
| Cit | Citrate |
| AKG | alpha-Ketoglutaric acid |
| SucCoA | Sucinyl-CoA |
| Suc | Succinate |
| GDP | GDP |
| GTP | GTP |
| Fum | Fumarate |
| FAD | FAD |
| FADH2 | FADH2 |
| Mal | Malate |
| Glu | Glutamate |
| NH3 | Ammonia |
| Ala | L-Alanine |
| Lac | Lactate |
| HCO3 | $HCO_3^-$ |
| NADP | $NADP^+$ |
| NADPH | NADPH |

| Reaction abbreviations | Reaction names |
|---|---|
| GLUT | Glucose transporter |
| GCK | Glucokinase |

| | |
|---|---|
| HK | Hexokinase |
| GPI | Glucose-6-phosphate isomerase |
| PFK | Phosphofructokinase |
| ALDO | Aldolase |
| TPI | Triosephosphate isomerase |
| GAPDH:PGK | Glyceraldehyde-3-phosphate dehydrogenase and Phosphoglycerate kinase |
| PGAM | Phosphoglycerate mutase |
| ENO | Enolase |
| PGM | Phosphoglucomutase |
| FBP | Fructose-1,6-bisphosphatase |
| G6PC | Glucose-6-phosphatase |
| GPD | Glycerol-3-phosphate dehydrogenase |
| PKLR | Pyruvate kinase |
| PDH | Pyruvate dehydrogenase |
| CS | Citrate synthase |
| ACO:IDH | Aconitase and Isocitrate dehydrogenase |
| OGDH | 2-Oxoglutarate dehydrogenase |
| LSC | Succinate-CoA ligase |
| SDH | Succinate dehydrogenase |
| FH | Fumarate hydratase |
| MDH | Malate dehydrogenase |
| GDH | Glutamate dehydrogenase |

| | |
|---|---|
| ALT | Alanine aminotransferase |
| LDH | Lactate dehydrogenase |
| MCT | Monocarboxylate transporter |
| PC | Pyruvate carboxylase |
| PCK | Phosphoenolpyruvate carboxykinase |
| ME | Malic enzyme |

38

## Introduction

Blood glucose homeostasis is crucial in mammals for providing stable energy sources to organs and maintaining health. During fasting, the liver plays a central role in maintaining blood glucose homeostasis by shifting its metabolism from glycolysis to gluconeogenesis (*1–5*). This metabolic shift is a highly regulated process that involves the directional reversal of metabolic reactions and fluctuations in the concentrations of numerous metabolites (*6–8*). Obesity induces metabolic dysregulation in the liver (*7–12*), leading to impaired glucose homeostasis (*13–17*) and the development of further diseases, including type 2 diabetes (*9*, *18–20*).

Metabolic processes are governed by the laws of thermodynamics. According to the second law of thermodynamics, in the cellular environment, metabolic reactions proceed in the direction where the Gibbs free energy change of reaction ($\Delta_r G'$) is negative, and $\Delta_r G'$ is zero when the reaction reaches equilibrium. Therefore, $\Delta_r G'$ indicates the reaction distance from equilibrium. $\Delta_r G'$ can be calculated as the difference between the Gibbs free energy of formation ($\Delta_f G'$) of the product and substrate metabolites:

$$\Delta_r G' = \sum_i S_i \Delta_f G_i' \tag{1}$$

where $S_i$ is the stoichiometric coefficient of metabolite *i* in the reaction. $\Delta_f G'$ depends on the metabolite activity, typically substituted by the concentration:

$$\Delta_f G' = \Delta_f G'^{\circ} + RT \ln c \tag{2}$$

57 where $\Delta_f G'^{\circ}$ is standard Gibbs free energy of formation representing $\Delta_f G'$ at 1M of
58 metabolite concentration, $R$ is the gas constant, $T$ is temperature, and $c$ is the metabolite
59 concentration. Although calculation of $\Delta_r G'$ requires absolute metabolite concentrations,
60 mass spectrometry-based metabolomics analyses often suffer from ion suppression, a
61 phenomenon where co-eluting compounds compromise quantitative accuracy by reducing
62 analyte ionization efficiency (*21*). Nevertheless, previous studies have successfully achieved
63 absolute quantification of intracellular metabolites, primarily by employing isotope-labeled
64 internal standards (*22*, *23*). These techniques have enabled the investigation of absolute
65 metabolite concentrations and subsequent thermodynamic analyses, such as $\Delta_r G'$
66 landscapes, in microorganisms and cultured cells. (*24–27*). Despite these advancements,
67 thermodynamic profiles have rarely been investigated at *in vivo* mammalian organ levels.
68 Furthermore, all prior thermodynamic studies have focused on glycolysis-dominant
69 conditions where glucose is the primary nutrient, leaving a large gap in our understanding of
70 metabolism during fasting, a condition dominated by gluconeogenesis.
71
72 Mathematical metabolic modeling is an essential framework for a quantitative system-level
73 understanding of metabolism. The thermodynamic principle regarding reaction direction has
74 been widely applied as a constraint to increase the reliability of metabolic models (*28–35*).
75 Furthermore, the significance of $\Delta_r G'$ extends beyond physical aspects such as distance
76 from equilibrium and reaction directionality to several physiological meanings, including
77 pathway rate-limiting steps quantified by the flux control coefficient (FCC) (*36–38*), and
78 enzyme demands for carrying metabolic flux (*39–42*). However, these thermodynamic

frameworks have hardly been applied to experimental data, especially those from multicellular organisms.

In this study, we explored $\Delta_r G'$ landscape in the liver metabolism of mice at different fasting levels using time-series absolute quantitative metabolomic data measured by CE-MS, which can reduce the effect of ion suppression (*43*, *44*), without using isotopically labeled standards. Our results are the first *in vivo* identification of large-scale $\Delta_r G'$ landscapes in mammalian organisms, and also the first elucidation of $\Delta_r G'$ behavior during fasting in any cell types. Since metabolomic data contains uncertainties, we developed GLEAM to estimate $\Delta_r G'$ with thermodynamically consistent metabolite concentrations from experimental metabolomic data. The estimated $\Delta_r G'$ showed that the global $\Delta_r G'$ landscape in mouse liver is robust during fasting, despite large fluctuations in metabolite concentrations. We further integrated the $\Delta_r G'$ and enzymatic kinetics to investigate the physiological significance of the $\Delta_r G'$ landscape in terms of rate-limiting steps and efficiency of metabolic switching. In addition to the thermodynamic robustness of mouse liver against fasting, we also demonstrated the robustness against obesity using leptin-deficient obese (*ob*/*ob*) mice (*45*, *46*). Thus, our study offers novel insights into glucose metabolism in *in vivo* mammalian liver from a thermodynamic standpoint. These findings extend our understanding of mammalian metabolisms beyond individual metabolite concentrations.

## Results

### $\Delta_r G'$ landscape is robust against fasting despite metabolite concentration fluctuations

In this study, we developed GLEAM to estimate $\Delta_r G'$ from time-series metabolome and $\Delta_f G'^{\circ}$. One of the challenges in estimating $\Delta_r G'$ in an entire reaction pathway is inherent uncertainties and missing values in metabolome and $\Delta_f G'^{\circ}$ data. To address this issue, GLEAM utilizes thermodynamic constraints and variances and covariances of metabolome and $\Delta_f G'^{\circ}$ data, and estimates a complete set of thermodynamically consistent metabolite concentrations and $\Delta_f G'^{\circ}$, and subsequent $\Delta_r G'$ (see Methods). Briefly, GLEAM fits metabolite concentrations and $\Delta_f G'^{\circ}$ to data from the experiment or database within a range that every reaction holds $\Delta_r G' < 0$ by the weighted least mean squares method. The weights of the residuals are determined by variances and covariances of metabolite concentrations and $\Delta_f G'^{\circ}$ data.

By applying GLEAM to time-series metabolomic data from *ad libitum* feeding to fasting in mice, and $\Delta_f G'^{\circ}$ data from eQuilibrator (data file S1), we estimated the $\Delta_r G'$ landscape (Fig. 1A, B, data file S2) in glycolysis, gluconeogenesis, and TCA cycle (data file S3) in the liver. At *ad libitum* feeding (0-hour fasting), when glycolysis is dominant, most of the irreversible reactions were markedly far from equilibrium, such as $\Delta_r G' = -21.56$ kJ/mol in PFK and $\Delta_r G' = -34.34$ kJ/mol in PDH. Among the 11 irreversible reactions, only three reactions (ACO:IDH, PC, and PCK) exhibited $\Delta_r G' > -10$ kJ/mol, and PC and PCK were exceptionally near equilibrium, with $\Delta_r G' = -3.48$ kJ/mol and $-3.70$ kJ/mol, respectively.

120 In contrast, most of the reversible reactions exhibited $\Delta_r G'$ close to zero at *ad libitum*
121 feeding, such as $\Delta_r G' = -0.24$ kJ/mol in GPI and $\Delta_r G' = -0.03$ kJ/mol in SDH, suggesting
122 that these reactions were near equilibrium. Four reversible reactions (ALDO, LSC, MDH,
123 and ME) were exceptions and exhibited $\Delta_r G' < -5$ kJ/mol. MDH was largely far from
124 equilibrium in the opposite direction of the oxidative TCA cycle, with $\Delta_r G' = -18.13$ kJ/mol.
125
126 The fasting-induced metabolic shifts in the liver from glycolysis to gluconeogenesis lead to
127 changes in thermodynamic characteristics of metabolic reactions, including reversal of the
128 sign of $\Delta_r G'$ of some reactions *i.e.* reversal of their direction. After 16-hour fasting, when
129 gluconeogenesis is dominant in the liver, all irreversible reactions exhibited $\Delta_r G' < -5$
130 kJ/mol, indicating that the overall trend of irreversible reactions being far from equilibrium
131 was maintained across *ad libitum* feeding and after fasting (Fig. 1C) despite large differences
132 in metabolite concentrations (Fig. 1D). Although PC and PCK had been near equilibrium at
133 *ad libitum* feeding, these reactions moved away from equilibrium to exhibit $\Delta_r G' = -9.07$
134 kJ/mol and −5.25 kJ/mol after fasting, respectively. As for reversible reactions, the directions
135 of some reactions are reversed to switch the liver's metabolism from glycolysis to
136 gluconeogenesis. However, all the reversible reactions with $\Delta_r G' > -5$ kJ/mol at *ad libitum*
137 feeding remained $\Delta_r G' > -5$ kJ/mol, indicating that the overall trend of reversible reactions
138 being close to equilibrium was maintained across *ad libitum* feeding and after fasting.
139
140 To examine whether the thermodynamic characteristics of metabolic reactions observed in
141 mouse liver are conserved across species, we compared the estimated $\Delta_r G'$ in glycolytic

142 reactions in mouse liver with those in other biological systems. The previous study (*26*)
143 determined $\Delta_r G'$ in glycolysis of immortalized baby mouse kidney epithelial (iBMK) cells,
144 yeast, and *Escherichia coli*. Similar to the mouse liver, all of these cell types showed
145 reversible reactions close to equilibrium, and the irreversible reaction PFK far from
146 equilibrium (Fig. 1E). This result suggests that the thermodynamic characteristics in
147 glycolysis are widely conserved across species. An exception is PKLR, whose $\Delta_r G'$ in
148 mouse liver was more than 20 kJ/mol smaller than those in the other cell types. Among the
149 metabolite concentrations (or ratios) involved in PKLR, pyruvate concentration and
150 ATP/ADP were smaller in mouse liver than in mammalian iBMK cells, yeast, and *E. coli*
151 (Table S2). In particular, pyruvate concentrations were two orders of magnitude smaller in
152 mouse liver ($3.77 \times 10^{-2}$ mM) compared to the other three cell types (5.88 mM in iBMK cells,
153 9.40 mM in yeast, and 3.66 mM in *E. coli*).
154

155 **$\Delta_r G'$ maintenance during fasting is associated with metabolite concentration**
156 **fluctuations in different ways among pathways**

157 To characterize thermodynamic changes in each metabolic reaction accompanying the
158 fasting-induced metabolic shift, we calculated the $\Delta_r G'_{16\mathrm{h}} - \Delta_r G'_{0\mathrm{h}}$ during fasting, defined
159 as $\Delta_r G'$ variations (Fig. 2A). Among the seven irreversible reactions of glycolysis and
160 gluconeogenesis, four reactions (GCK, PFK, PKLR, and PC) exhibited an absolute $\Delta_r G'$
161 variation during fasting greater than 5 kJ/mol. In contrast, only one reversible reaction
162 (ALDO) out of 11 showed an absolute $\Delta_r G'$ variation during fasting exceeding 5 kJ/mol,
163 despite the reversal of reversible reaction directions between glycolysis and gluconeogenesis
164 under these conditions. This result suggests that reversible reactions maintained $\Delta_r G'$ more
165 strictly than irreversible reactions even though the sign of $\Delta_r G'$ is reversed. In the TCA
166 cycle, the absolute $\Delta_r G'$ variations during fasting were less than 3 kJ/mol for all reactions,
167 indicating that the TCA cycle is thermodynamically stable in response to fasting.

168

169 As $\Delta_r G'$ variations during fasting differed between irreversible and reversible reactions in
170 glycolysis and gluconeogenesis, we further examined the relationship between the distance
171 from equilibrium ($|\Delta_r G'|$) at *ad libitum* feeding and the absolute $\Delta_r G'$ variation (Fig. 2B).
172 In glycolysis and gluconeogenesis, the absolute $\Delta_r G'$ variations during fasting were less
173 than 3.5 kJ/mol for near-equilibrium reactions with $|\Delta_r G'| < 5$ kJ/mol at *ad libitum* feeding
174 except for PC. PC moved away from equilibrium only when gluconeogenesis is dominant in
175 response to fasting. In contrast, among the reactions with $|\Delta_r G'| \geq 5$ kJ/mol at *ad libitum*
176 feeding, the absolute $\Delta_r G'$ variations ranged approximately between 0 and 10 kJ/mol. This

177 result suggests that $\Delta_r G'$ of near-equilibrium reactions in glycolysis and gluconeogenesis
178 tended to be significantly strictly maintained, while this tendency was lost among reactions
179 displaced from equilibrium (p value = 0.037 < 0.05 calculated by two-tailed Welch's *t*-test, n
180 = 12 for near-equilibrium reactions with $|\Delta_r G'| < 5$ and n = 6 for the other reactions with
181 $|\Delta_r G'| \geq 5$ kJ/mol). In the TCA cycle, $\Delta_r G'$ was strictly maintained regardless of the distance
182 from equilibrium. The statistical test was not performed for the TCA cycle due to a lack of
183 near-equilibrium reactions.
184
185 To investigate the reason maintaining $\Delta_r G'$ in near-equilibrium reactions in glycolysis and
186 gluconeogenesis, as well as in the TCA cycle reactions, we compared the absolute $\Delta_r G'$
187 variation with the total absolute $\Delta_f G'$ variation of metabolites involved in the reaction (Fig.
188 2C). The total absolute $\Delta_f G'$ variation of metabolites is defined as $\sum\left|S\left(\Delta_f G'_{16\mathrm{h}} - \Delta_f G'_{0\mathrm{h}}\right)\right|$,
189 where *S* is the stoichiometric coefficient of a metabolite involved in the reaction. The $\Delta_r G'$
190 variation is associated in various ways with fluctuations in the $\Delta_f G'$ of substrates and
191 products, which depend on the metabolite concentrations. For example, when substrate and
192 product concentrations remain relatively constant and changes in their $\Delta_f G'$ remain small,
193 the $\Delta_r G'$ variation is small (*e.g.*, GPD in Fig. 2D). Even when substrate and product
194 concentrations largely fluctuate and changes in their $\Delta_f G'$ are large, the $\Delta_r G'$ variation can
195 remain small when the changes in $\Delta_f G'$ of substrate and products are cancelled out. This
196 can happen, for instance, when both the substrate and product $\Delta_f G'$ values increase
197 simultaneously (*e.g.*, GAPDH:PGK in Fig. 2D). In contrast, when the changes in $\Delta_f G'$ of

198 substrate and products are not cancelled out, the $\Delta_r G'$ variation becomes large (*e.g.*, GCK
199 in Fig. 2D). In glycolysis and gluconeogenesis, reactions with small absolute $\Delta_r G'$ variation
200 due to small fluctuation in metabolite concentrations, such as GPD, and due to the
201 cancellation of $\Delta_f G'$ variations such as GAPDH:PGK, were both observed (Fig. 2C). The
202 existence of the latter type of reaction suggests that while metabolite concentrations fluctuate
203 in response to fasting in glycolysis and gluconeogenesis, the fluctuations in metabolites
204 involved in near-equilibrium reactions were coordinated, thereby maintaining $\Delta_r G'$ of these
205 reactions. In the TCA cycle, the reason for maintaining the absolute $\Delta_r G'$ variations were
206 small fluctuations in metabolite concentrations for all the reactions.
207

208 **Thermodynamic Rate-limiting candidates (TRCs) were maintained during fasting**

209 One of the physiological consequences of reaction distances from equilibrium is the control
210 of steady-state pathway fluxes. The extent to which perturbation of each reaction can control
211 pathway steady-state flux is quantified by the flux control coefficient (FCC) in metabolic
212 control analysis (MCA) (*36*, *47*). In this study, we analytically calculated FCCs under both
213 arbitrary $\Delta_r G'$ landscapes and those observed in mouse liver within glycolysis (Fig. 3A),
214 gluconeogenesis (Fig. 3B), and the TCA cycle (Fig. 3C) from an enzymatic rate law using
215 the MCA's theorems. To incorporate reaction distance from equilibrium, we used reversible
216 kinetics called the direct binding modular rate law (*48*) as the enzymatic rate law. Under this
217 framework, a flux $v$ can be decomposed into the effect of non-equilibrium $\eta_{\mathrm{rev}}$ (Fig. 3D)
218 and substrate saturation $\eta_{\mathrm{sat,s}}$ (*49*):

$$v = E k_{\mathrm{cat}}^{+} \eta_{\mathrm{rev}} \eta_{\mathrm{sat,s}}, \tag{3}$$

$$\eta_{\mathrm{rev}} = 1 - \exp\left(\frac{\Delta_r G'}{RT}\right), \tag{4}$$

$$\eta_{\mathrm{sat,s}} = \frac{\prod_{i \in M^{\mathrm{s}}} \left(\frac{c_i}{K_{\mathrm{m},i}}\right)^{|s_i|}}{1 + \prod_{i \in M^{\mathrm{s}}} \left(\frac{c_i}{K_{\mathrm{m},i}}\right)^{|s_i|} + \prod_{i \in M^{\mathrm{p}}} \left(\frac{c_i}{K_{\mathrm{m},i}}\right)^{|s_i|}} \tag{5}$$

219 where $E$ is an enzyme concentration, $k_{\mathrm{cat}}^{+}$ is the forward catalytic constant, $K_{\mathrm{m}}$ is the
220 Michaelis-Menten constant, $M^{\mathrm{s}}$ is substrates, and $M^{\mathrm{p}}$ is products. Using this reaction rate
221 raw, we calculated FCC based on the connectivity theorem and summation theorem in MCA
222 (*50*) (see Methods). This FCC calculation depends on metabolite concentrations, $\Delta_f G'^{\circ}$, and
223 $K_{\mathrm{m}}$. For $\Delta_f G'^{\circ}$, we used sampling values for the confidence interval calculation in GLEAM.

224 $K_{\mathrm{m}}$ values were sampled from distributions based on BRENDA database data (*51*).
225 Metabolite concentrations were obtained by the following two approaches.
226
227 We investigated FCC for metabolite concentrations in mouse liver using sampled values for
228 confidence interval calculations in GLEAM, and FCC for arbitrary $\Delta_r G'$ landscapes to
229 identify thermodynamic conditions for large FCC. FCC for arbitrary $\Delta_r G'$ landscapes
230 showed that moderate or large FCC required $\eta_{\mathrm{rev}} \approx 1$ in reactions except for ones located
231 upstream in a pathway (Fig. S1 A to D). In glycolysis, reactions with $\eta_{\mathrm{rev}} \approx 1$ at *ad libitum*
232 feeding included irreversible reactions GCK, PFK, PKLR, and the reversible reaction ALDO
233 in mouse liver. Among these, reactions that can achieve FCC ≈ 1 were GCK and PFK, while
234 others can achieve at most moderate FCC values (Fig. 3E). We also found that GPI, which is
235 located upstream in the pathway, can achieve moderate FCC at moderate $\eta_{\mathrm{rev}}$. In
236 gluconeogenesis, reactions with $\eta_{\mathrm{rev}} \approx 1$ after 16-hour fasting were the irreversible
237 reactions PC, PCK, FBP, and G6PC, all of which can achieve FCC ≈ 1 (Fig. 3F). All the other
238 reactions exhibited only small FCC values. In the TCA cycle, similar FCC distributions were
239 observed at *ad libitum* feeding and after fasting (Fig. 3G, S3). Reactions with $\eta_{\mathrm{rev}} \approx 1$ were
240 irreversible reactions CS, ACO:IDH, OGDH, and a reversible reaction LSC. Among these,
241 CS and OGDH can achieve FCC ≈ 1, while ACO:IDH and LSC can achieve at most moderate
242 FCC values. Generally, reversible reactions are considered to exhibit only small FCC values
243 and thus are not recognized as rate-limiting reactions. However, our results demonstrated that
244 the reversible reactions GPI, ALDO, and LSC can achieve moderate FCC values comparable
245 to several irreversible reactions. Considering the results of arbitrary $\Delta_r G'$ landscapes, these

246 FCC values of the reversible reactions can be attributed to GPI being located relatively
247 upstream in glycolysis, and ALDO and LSC being sufficiently displaced from equilibrium to
248 achieve $\eta_{\mathrm{rev}} \approx 1$ despite being closer to equilibrium than irreversible reactions.
249
250 As described above, a reaction with a large FCC seems to be either far from equilibrium ($\eta_{\mathrm{rev}}$
251 $\approx 1$), or located upstream in a pathway. Because the location of a reaction in a pathway
252 depends on the definition of the pathway, a reaction being far from equilibrium is a key
253 determinant for the reaction to have a large FCC, sometimes being referred to as the rate-
254 limiting step. Therefore, we introduced Thermodynamic Rate-limiting Candidates (TRC) as
255 reactions with $\eta_{\mathrm{rev}} \geq 0.9$, and examined which reaction is thermodynamically capable of
256 being a rate-limiting step for any pathway definitions at *ad libitum* feeding (Fig. 3H, 0h) and
257 after fasting (Fig. 3H, 16h). TRC reactions both at *ad libitum* feeding and after fasting
258 included GCK, PFK, CS, and seven other reactions, indicating these reactions can be a rate-
259 limiting step regardless of fasting levels. The parameter $\eta_{\mathrm{rev}}$ and TRC status (either TRC
260 or not) are sensitive to $\Delta_r G'$ variations at a near equilibrium because $\eta_{\mathrm{rev}}$ saturates around
261 $\Delta_r G' = -10$ kJ/mol (Fig. 3D). Due to this property, 15 out of 18 reactions remained either
262 TRC (red line in Fig. 3H) or non-TRC (blue line in Fig. 3H) across at *ad libitum* feeding and
263 after fasting in glycolysis and gluconeogenesis, where only $\Delta_r G'$ of near-equilibrium
264 reactions were strictly maintained. This result suggests that fasting-induced fluctuations in
265 metabolite concentrations occur within a range that maintains the TRC status for most
266 reactions. The three reactions of ALDO, PC, and PCK were the exceptions that did not remain
267 TRC or non-TRC (gray line in Fig. 3H), and whether these reactions are rate-limiting or not

would depend on fasting levels. TRC status described above remains stable across the threshold from $\eta_{\mathrm{rev}}$ = 0.88 to 0.95.

**Glycolysis and Gluconeogenesis Achieve Efficient Directional Switching by Expending Large Enzyme Costs**

A fundamental question in biology is to understand what biological systems are optimized for. While objective functions optimized in microbial metabolism—such as maximizing growth or ATP production (*52*) and minimizing enzyme demands (*42*)—have been reported, the objective function for *in vivo* mammalian metabolism remains completely unknown. Therefore, we examined the optimality of metabolism in mouse liver from the aspect of metabolite concentrations and $\Delta_r G'$ landscape obtained from GLEAM.

By solving the equation of the direct binding modular rate law (1) with respect to the enzyme amount, we obtain

$$E = \frac{v}{k_{\mathrm{cat}}^{+}} \eta_{\mathrm{rev}}^{-1} \eta_{\mathrm{sat,s}}^{-1}. \tag{6}$$

This equation shows that the nearer a reaction is to equilibrium (the smaller $\eta_{\mathrm{rev}}$ is), the greater the enzyme amount required to achieve the same flux $v$. Here we defined Enzyme Cost (EC) as the product of enzyme amount and enzyme molecular weight, and Enzyme Cost Minimum (ECM) as the theoretical state that minimizes the total EC within the entire pathway (see Method). By comparing ECs and metabolite concentrations in mouse liver to those in ECM, we investigated whether mouse liver metabolism is optimized for enzyme demands reduction. As with FCC calculation, we calculated EC using sampling values of metabolite concentrations and $\Delta_f G'^{\circ}$ used in the confidence interval calculation in GLEAM. For $K_{\mathrm{m}}$ values, we obtained them as geometric means of data in the BRENDA database (*51*).

291

292 We calculated EC and ECM for the reactions in glycolysis at *ad libitum* feeding,
293 gluconeogenesis after 16-hour fasting, and the TCA cycle under both these conditions (data
294 file S4). The liver showed larger total EC compared to ECM, with a difference between
295 pathways. The liver/ECM ratio of total EC was on the order of $10^4$ for glycolysis and
296 gluconeogenesis, but only $10^1$ for the TCA cycle (Fig. 4A). Additionally, we compared ECM-
297 predicted metabolite concentrations with liver metabolite concentrations in each pathway,
298 and found typical fold errors of $10^{RMSE} = 29.79$ (RMSE: root mean square error on a $\log_{10}$-
299 scale) for glycolysis and gluconeogenesis and 14.40 for the TCA cycle (Fig. 4B). These
300 findings show that enzyme and metabolite concentrations in the liver are not optimized for
301 EC, and this is more evident in glycolysis and gluconeogenesis than in the TCA cycle.

302

303 To identify a key reaction contributing to the large total EC of glycolysis and gluconeogenesis
304 in mouse liver, we broke down the total EC of pathways into ECs of individual reactions
305 (data file S4). The GAPDH:PGK reaction in mouse liver exhibited the highest EC of $10^6$ both
306 in glycolysis and gluconeogenesis (Fig. 4C), while EC of reactions in the TCA cycle (*e.g.*,
307 SDH, ACO:IDH, and FH) are at most on the order of $10^2$. The EC values of GAPDH:PGK
308 are 99% and 89% of the total EC of glycolysis and gluconeogenesis, respectively, suggesting
309 that GAPDH:PGK outstandingly elevates the total EC of glycolysis and gluconeogenesis.
310 The high EC for GAPDH:PGK both in glycolysis and gluconeogenesis is attributed to two
311 factors. One factor is low substrate saturation (Fig. 4C, blue), which is given by the lower
312 substrate metabolite concentrations ($3.4\times10^{-3}$ mM of GAP *ad libitum* feeding and $1.3\times10^{-2}$

313 mM of 3PG after fasting) than their respective $K_{\mathrm{m}}$ values ($1.9\times10^{-1}$ mM for GAP and
314 $3.5\times10^{-1}$ mM for 3PG), resulting in large $\eta_{\mathrm{sat,s}}^{-1}$. From equation (4), a large $\eta_{\mathrm{sat,s}}^{-1}$, indicating
315 low substrate saturation, leads to an increase in EC to carry a certain flux. Under this
316 condition, an increase in flux from higher enzyme levels is mitigated by fluctuations in
317 metabolite concentrations. The other factor of the high EC for GAPDH:PGK is liver
318 thermodynamics (Fig. 4C, red), where the reaction was close to equilibrium ($\Delta_r G' = -0.01$
319 kJ/mol both at *ad libitum* feeding and after fasting), resulting in large $\eta_{\mathrm{rev}}^{-1}$. When the reaction
320 is close to equilibrium, increasing the enzyme abundance enhances both the forward and
321 reverse fluxes, thus limiting the net flux increase. Thus, the elevated EC for this reaction is a
322 result of both low substrate saturation and high reaction reversibility.
323
324 The liver glycolysis and gluconeogenesis required much larger EC than ECM, especially in
325 the midstream reversible reactions due to large $\eta_{\mathrm{rev}}^{-1}$ values. We hypothesized that the reason
326 for this may be that the enzyme costs are required for enabling switching from glycolysis to
327 gluconeogenesis during fasting. To assess the metabolic hurdle for directional switching from
328 glycolysis to gluconeogenesis, we introduced the Metabolite Equilibrium Gap (MEG) as the
329 typical fold change in metabolite concentration required for the directional switching (data
330 file S5) (see Methods). In glycolysis and gluconeogenesis, mouse liver exhibited MEG =
331 1.35 while ECM exhibited MEG = 16.01 (Fig. 4D), suggesting that the liver achieves
332 directional switching from glycolysis to gluconeogenesis with much smaller metabolite
333 concentration changes than ECM. Unlike glycolysis and gluconeogenesis, the TCA cycle,
334 which does not undergo directional switching during fasting, exhibited a larger MEG (6.85)

in the liver than that of glycolysis and gluconeogenesis. The mouse liver expends a much larger enzyme cost in glycolysis and gluconeogenesis than the theoretical minimum, allowing it to achieve directional switching with smaller changes in metabolite concentration. Conversely, a smaller enzyme cost is expended for the TCA cycle—which does not undergo directional switching—than for glycolysis and gluconeogenesis.

341 **Robustness of $\Delta_r G'$ in The Liver Against Obesity**

342 Obesity disrupts liver metabolism, leading to impaired homeostasis in response to fasting (*7*,
343 *8*, *10*) and subsequent development of various diseases (*9*, *18–20*). Recent studies have
344 reported that the obesity-associated dysregulation of liver metabolism occurs even at *ad*
345 *libitum* feeding (*11*, *12*). To reveal the impact of obesity-induced metabolic disruption on the
346 thermodynamic characteristics of reactions, we calculated $\Delta_r G'$ in the *ob*/*ob* mouse liver
347 during fasting.

348

349 The $\Delta_r G'$ landscape in *ob*/*ob* mouse liver was similar to that in WT mouse liver both at ad
350 libitum feeding and after 16-hour fasting (Pearson's correlation coefficient $r$ = 0.99 at ad
351 libitum feeding and 0.98 after 16-hour fasting) (Fig. 5A, B, data file S2). Consequently, the
352 overall trend of irreversible reactions being far from equilibrium and reversible reactions
353 being near equilibrium was preserved even under obesity. More than 80% of all 29 reactions
354 showed markedly small $\Delta_r G'$ differences (less than 3 kJ/mol) between WT and *ob*/*ob* mice
355 both at *ad libitum* feeding and after 16-hour fasting, with only three reactions (TPI after 16-
356 hour fasting, CS at the both timepoints) exceeding a 5 kJ/mol differences (Fig. 5C). The
357 similar $\Delta_r G'$ values between WT and *ob*/*ob* mouse indicate that the concentration ratios of
358 substrates and products for the reactions are comparable between the genotypes. Individual
359 metabolite concentrations (data file S2), however, showed discrepancies between WT and
360 *ob*/*ob* mice, with Pearson's $r$ = 0.015 at ad libitum feeding and −0.46 after 16-hour fasting
361 (Fig. 5D). This result suggests that the thermodynamic characteristics of reactions remain
362 robust against obesity despite the changes in individual concentrations. Particularly, in most

363 reversible reactions of glycolysis and gluconeogenesis, the differences in $\Delta_f G'$ between WT
364 and *ob*/*ob* mouse were not reflected in the differences in $\Delta_r G'$ (Fig. 5E). This result
365 prominently demonstrates that the reaction thermodynamic characteristics are robust to
366 obesity while the individual metabolite concentrations are sensitive.
367

368 **Discussion**

369 We revealed the $\Delta_r G'$ landscape of glucose metabolism in *in vivo* mouse liver for the first
370 time from fasting time-series absolute quantitative metabolome data using the newly
371 developed GLEAM. In mouse liver, overall trend of $\Delta_r G'$ landscape was maintained
372 regardless of fasting level (Fig. 1B, C). The $\Delta_r G'$ maintenance was markedly strict in near-
373 equilibrium reactions in glycolysis and gluconeogenesis such as GAPDH:PGK (Fig. 2B),
374 despite large fluctuations in metabolite concentrations (Fig. 1D, 2C), while this strictness was
375 not true for reactions far from equilibrium such as GCK. In the TCA cycle, overall $\Delta_r G'$
376 variations were small due to minimal metabolite concentration fluctuations during fasting
377 (Fig. 2B, C). This thermodynamic robustness against fasting led to maintenance of the
378 reactions that could have large FCC (*i.e.*, rate-limiting step candidates) during fasting (Fig.
379 3H) because FCC is sensitive only in the near-equilibrium region. The thermodynamic
380 landscape in the liver could also contribute to an efficient switching from glycolysis to
381 gluconeogenesis by expending a larger enzyme expression than that theoretically minimized
382 (Fig. 4A to D). We also found similar $\Delta_r G'$ landscapes between WT and *ob*/*ob* mice, while
383 metabolite concentrations were quite different (Fig. 5A to E). Our results revealed that the
384 liver robustly maintains $\Delta_r G'$ landscapes favorable for metabolic control in contrast to
385 fluctuations in individual metabolite concentrations caused by fasting and obesity.

386

387 Methods for estimating thermodynamically consistent metabolite concentrations, $\Delta_f G'^{\circ}$, and
388 $\Delta_r G'$ from absolute quantitative metabolome data have been proposed in previous studies
389 (*26*, *27*). In these methods, metabolite concentrations and $\Delta_f G'^{\circ}$ were determined by

390 weighted least squares, where uncertainties of individual concentration or $\Delta_f G'^\circ$ were
391 independently accounted with the weights. However, metabolites sharing common chemical
392 group, such as ADP and ATP, show high correlation in their $\Delta_f G'^\circ$, because $\Delta_f G'^\circ$ depends
393 on structures of metabolites. GLEAM incorporates the covariance of $\Delta_f G'^\circ$ from
394 eQuilibrator (*53*) and enabled more precise $\Delta_r G'$ estimation compared to the previous
395 methods.
396
397 Our study narrowed down the reactions that could achieve large FCC in the pathways using
398 the obtained $\Delta_r G'$ landscape in mouse liver (Fig. 3E to G, S2). A previous study
399 experimentally measured FCC in glycolysis in iBMK cells, and reactions exhibiting large
400 FCCs are hexokinase (HK), which catalyzes the same reaction as GCK, and PFK (*54*).
401 Another previous study exhibited PC having dominant FCC in gluconeogenesis in rat liver
402 (*55*, *56*). Although no studies have measured FCC in the TCA cycle to our knowledge, CS,
403 IDH, and OGDH have conventionally been regarded as rate-limiting steps. All these reactions
404 are included in the rate-limiting candidates in this study, suggesting that rate-limiting
405 reactions are maintained through cell types. However, the advantage of controlling flux via
406 these reactions remains unclear and is an important future topic for understanding system-
407 level metabolic regulation.
408
409 When calculating EC, we made two assumptions: having common turnover number, $k_{\mathrm{cat}}$
410 values for all reactions and setting saturation ($c/K_{\mathrm{m}}$) to the geometric mean of the pathway
411 when $K_{\mathrm{m}}$ could not be obtained from BRENDA. These assumptions were required because

412 of the difficulty of obtaining kinetic parameters in mammals. The former assumption may
413 cause inaccurate weighting of individual enzymes in the total EC minimization, and the latter
414 may lead to inaccurate $\eta_{\mathrm{sat,s}}^{-1}$. However, the metabolite concentrations close to ECM were
415 reported with a modeling where $k_{\mathrm{cat}}$ and $K_{\mathrm{m}}$ information was lacking and only the
416 influence of $\eta_{\mathrm{rev}}^{-1}$ was considered (*42*). This means that the $\Delta_r G'$ landscape in ECM would
417 be similar under any $k_{\mathrm{cat}}$ and $K_{\mathrm{m}}$ values. Therefore, our conclusion of mouse liver
418 metabolism not being optimized for enzyme cost reduction would be reasonable regardless
419 of $k_{\mathrm{cat}}$ and $K_{\mathrm{m}}$ assumptions.
420
421 According to equations (23), (24), (30) to (35), and (39), the design of $\Delta_r G'$ landscape faces
422 a trade-off between FCC concentration and enzyme cost minimization. If only a few reactions
423 in a metabolic pathway are far from equilibrium and exhibit $\eta_{\mathrm{rev}}$ close to 1, large FCCs are
424 likely to be concentrated in these reactions. In this case, $\eta_{\mathrm{rev}}$ of other reactions are close to
425 zero, leading to a large EC. This trade-off can be rephrased as a trade-off between flexibility
426 responding to multiple conditions and survival cost reduction under a single condition
427 because the pathway flux can be efficiently regulated through a minimal number of enzyme
428 activity changes when FCCs are concentrated in limited reactions. A similar trade-off also
429 occurs between MEG reduction and enzyme cost minimization. In mouse liver, particularly
430 in glycolysis and gluconeogenesis, reactions that could achieve high FCC were concentrated
431 in a few reactions (Fig. 3E to G, S2), and MEG was remarkably small (Fig. 4D), while there
432 were large deviations between mouse liver and ECM in total EC and metabolite
433 concentrations (Fig. 4A, B). These results indicate that metabolic regulation in mouse liver

434 adopts a strategy of flexibly responding to changes in environmental and physiological
435 conditions rather than optimizing for a certain condition. In contrast, the previous study in *E.*
436 *coli* showed that both enzyme concentrations and metabolite concentrations are well
437 predicted by ECM within a typical fold error range of $10^0$ (*42*) (Fig. S3). Taken together,
438 these facts suggest differences in metabolic regulation strategies between cell types; mouse
439 liver expends costs to perform flexible metabolic regulation, while *E. coli* optimized survival
440 cost in a certain condition. Furthermore, our study also showed that this difference in
441 metabolic regulation strategy may also exist between pathways by demonstrating the large
442 differences in TRC proportions and total EC optimality between glycolysis and
443 gluconeogenesis, and the TCA cycle. Note that the different total EC optimality among cell
444 types and pathways is consistent with their common tendency of reversible reactions being
445 near equilibrium (Fig. 1A, B) because $\eta_{\mathrm{rev}}^{-1}$ reaches $10^2$ at $\Delta_r G' = -5$ kJ/mol, meaning EC
446 takes greatly different values even in the range of near equilibrium.
447
448 One of the limitations of this study is that we assumed hepatocytes as a single compartment
449 and calculated $\Delta_r G'$ from metabolite concentrations averaged within the cell. As glycolysis
450 operates in the cytosol and the TCA cycle operates in mitochondria, more accurate $\Delta_r G'$
451 calculation requires concentrations in each of these compartments. Furthermore, localized
452 concentrations can be affected by substrate channeling (*57*). Substrate channeling is a
453 phenomenon where enzymes of consecutive reactions form complexes, allowing the product
454 of the former enzyme to be directly transferred to the active site of the latter enzyme without
455 being released into the solvent. For reactions involved in substrate channeling, $\Delta_r G'$ is

456 dependent on the channeled metabolite concentration in a limited space among the enzymes.
457 Although substrate channeling has not yet been confirmed in living organisms, the
458 channeling of oxaloacetate between MDH and CS has been indirectly supported by
459 experiments (*58*, *59*), and ALDO, TPI, and GAP have also been suggested to form complexes
460 (*60*, *61*). Another limitation is that the FCC calculations were based solely on stoichiometric
461 relationships and did not account for allosteric regulations because of the severe lack of $K_{\mathrm{i}}$
462 in mammals and simplification of the calculation. Inclusion of allosteric regulations would
463 alter FCC values, allowing for further narrowing down the reactions that can have a large
464 FCC.
465
466 In conclusion, we developed GLEAM to estimate $\Delta_r G'$ in the glucose metabolism in mouse
467 liver and revealed the thermodynamic robustness against fasting and obesity. Furthermore,
468 we suggested that these thermodynamic characteristics in the liver contribute to efficient
469 metabolic control in two ways: the maintenance of rate-limiting step candidates and the
470 switching between glycolysis and gluconeogenesis with minimal metabolite fluctuations by
471 expending large enzyme expressions. This study thus provides crucial insights into the
472 principles underlying the highly flexible and robust metabolic regulation observed in
473 mammalian liver, paving the way for future investigations into therapeutic targets for
474 metabolic diseases.
475

476 **Materials and Methods**

477 **Metabolic network for glucose metabolism in mice**

478 A metabolic network for glucose metabolism in mice was constructed to calculate $\Delta_r G'$. The
479 network consists of total 55 reactions and 80 metabolites in the liver, muscle, and blood (the
480 same reactions and metabolites in different compartments were counted as distinct ones), and
481 involves glycolysis, gluconeogenesis, TCA cycle, glycogen metabolism, alanine metabolism,
482 and transporters (Fig. S4, data file S3). Among the 55 reactions, we defined 23 reversible
483 reactions and 32 irreversible reactions based on the tissue-specific genome-scale metabolic
484 network (*62*). All the transporters were defined as reversible reactions.

485

486 Reversible reactions GAPDH and PGK were combined into a single reversible reaction
487 GAPDH:PGK because 1,3-bisphosphoglycerate was not measured in the metabolomic data
488 (*8*). According to the experimentally measured metabolite concentrations, a reversible
489 reaction ACO proceeded in the reverse direction of the oxidative TCA cycle with a little
490 thermodynamic driving force at all the time points in WT and *ob*/*ob* mice, breaking a
491 sequential pathway from CS to FH. Since this long sequential pathway is necessary for the
492 downstream analysis, such as FCC and MEC calculation, we summed ACO and irreversible
493 reaction, IDH, which have a large thermodynamic driving force in the direction of the
494 oxidative TCA cycle, as a single irreversible reaction, ACO:IDH.

495

496 In the skeletal muscle, FBP, G6PC, and PCK in gluconeogenesis were not included in the
497 metabolic network. Although PC is also involved in gluconeogenesis, PC is included in the

metabolic network of skeletal muscle because we could not exclude the possibility of its expression in the skeletal muscle (*63*, *64*).

In this study, we assumed the liver and skeletal muscle as a single compartment of hepatocytes and myocytes, respectively, and cytosolic and mitochondrial compartments in these cells were not considered for simplification of the modeling. Therefore, the $\Delta_r G'$ calculated in this study represents the average values within the cells.

**Algorithm of GLEAM**

We developed GLEAM as a method to estimate complete set of thermodynamically consistent metabolite concentrations and $\Delta_f G'^{\circ}$ values, from metabolomic data on a logarithmic scale, $\mathbf{ln}\,\boldsymbol{c} \in \mathbb{R}^{m \times h \times g}$, and $\Delta_f G'^{\circ}$ data calculated by the component contribution method (*65*), $\boldsymbol{\Delta_f G'^{\circ}} \in \mathbb{R}^{m}$, where $m$, $h$, $g$ are the number of metabolites, timepoints, and genotypes, respectively. Since metabolomic and $\Delta_f G'^{\circ}$ data contain uncertainties and missing values, directly substituting them into the definition equation of $\Delta_r G'$ often violates the second law of thermodynamics. To address this issue, GLEAM corrects for the uncertainties and missing values by calculate the most plausible values based on measured metabolomic data within a thermodynamically feasible space.

We first formulate the quadratic programming problem to minimize the departures of estimated metabolite concentrations and $\Delta_f G'^{\circ}$ from the experimental and database values under thermodynamic and physiological constraints:

$$\min_{y \in \{\ln c, \Delta_f G'^\circ\}, a} Z_{\mathrm{QP}}$$

$$= \sum_{y} \frac{1}{\# y^{\mathrm{exp}}} \left\{ (\boldsymbol{y} + \boldsymbol{a} - \boldsymbol{y}^{\mathbf{exp}})^{\mathrm{T}} \boldsymbol{\Sigma}_{(y)}^{-1} (\boldsymbol{y} + \boldsymbol{a} - \boldsymbol{y}^{\mathbf{exp}}) + \sum_{i} \lambda \left| \frac{(\boldsymbol{P}_i)^{\mathrm{T}} \boldsymbol{a}}{\sqrt{D_{ii}}} \right| \right\}$$

$$\text{s.t.} \qquad \Delta_r G'_j < 0 \quad \forall i \in M, \forall j \in N$$

$$\Delta_r G'_j = \sum_{i \in M} S_{i,j} \left( \Delta_f G'^\circ_i + RT \ln c_i \right) \quad \forall j \in N^{\mathrm{cell}}$$

$$\Delta_r G'_{\mathrm{GLUT}} = RT \ln \frac{[\mathrm{Glu[h]}]}{[\mathrm{Glu[b]}]} \tag{7}$$

$$\Delta_r G'_{\mathrm{LDH}} = RT \ln \frac{[\mathrm{H^+[b]}][\mathrm{Lac[b]}]}{[\mathrm{H^+[h]}][\mathrm{Lac[h]}]}$$

$$b_i \leq \ln c_i \leq ub_i \quad \forall i \in M$$

$$b_i \leq \ln \frac{c_{i_1}}{c_{i_2}} \leq ub_i \quad \forall (i_1, i_2) \in M^{\mathrm{cofactor}}$$

where $c_i$ is concentration of metabolite $i$, $S_{ij}$ is stoichiometric coefficient of metabolite $i$ in reaction $j$, $R$ is gas constant, and $T$ is temperature. $M$, $N$, and $N^{\mathrm{cell}}$ are sets of metabolites, reactions, and intracellular reactions, respectively. $M^{\mathrm{cofactor}}$ is the cofactor pairs of which the ratio was constrained. $\boldsymbol{\Sigma}$ is variance-covariance matrix of which the eigen decomposition is $\boldsymbol{\Sigma} = \mathbf{PDP}^{\mathrm{T}}$. $a$ is systematic error, and $\lambda$ is regularization parameter. The superscript exp means measured or database value. The first term in curly brackets of the objective function represents the variance and covariance-weighted residuals of estimated metabolite concentrations and $\Delta_f G'^\circ$, which considers systematic errors from experimental operations, while the second term represents a regularization term for systematic errors to avoid overfitting. By using the covariances in $\Delta_f G'^\circ$ for the weight of residuals, the

estimation reflects the correlations in $\Delta_f G'^{\circ}$ due to shared chemical groups. In contrast, all covariances between metabolite concentrations were set to zero, making $\boldsymbol{\Sigma}$ a diagonal matrix, since no prior correlation in metabolite concentrations is expected.

The solution of the optimization problem (7) may not provide unique concentrations, especially for unmeasured metabolites, which can lead to undetermined $\Delta_r G'$ of the reactions involving the unmeasured metabolites. To estimate unique $\Delta_r G'$, two terms with variance of unmeasured metabolite concentrations were added to the objective function:

$$\begin{aligned} Z_{\mathrm{QP_unique}}(y,a) = & \sum_{y} \frac{1}{\#y^{\mathrm{exp}}} \left\{ (\boldsymbol{y}+\boldsymbol{a}-\boldsymbol{y}^{\mathbf{exp}})^{\mathrm{T}} \boldsymbol{\Sigma}_{(y)}^{-1} (\boldsymbol{y}+\boldsymbol{a}-\boldsymbol{y}^{\mathbf{exp}}) + \sum_{i} \lambda \left| \frac{(\boldsymbol{P}_i)^{\mathrm{T}} \boldsymbol{a}}{\sqrt{D_{ii}}} \right| \right\} \\ & + \epsilon_1 \sum_{(h_1,h_2)\in H^{\mathrm{adj}}} \frac{1}{(h_2-h_1)} \sum_{i\in M^{\mathrm{unmeasured}}} \left(\ln c_{i,h_2} - \ln c_{i,h_1}\right)^2 \\ & + \epsilon_2 \sum_{i\in M^{\mathrm{unmeasured}}} \left(\ln c_i - \widehat{\ln c_i}\right)^2 \end{aligned} \tag{8}$$

where $H^{\mathrm{adj}}$ is pairs of adjacent timepoints, $M^{\mathrm{unmeasured}}$ is unmeasured metabolites, $\widehat{\ln c}$ is median of upper and lower bounds of metabolite concentration, and $\epsilon_1$ is small values enough to prioritize the first term over the second term. Similarly, $\epsilon_2$ ($\epsilon_1 \gg \epsilon_2$) allows the second term to take precedence over the third term. The second term of the objective function (the first additional term) reduces the sum of concentration changes of unmeasured metabolites across time points, making smooth concentration changes more likely to be estimated than unnatural repetition of increases and decreases. The third term of the objective function (the second additional term) departures of the estimated unmeasured metabolite concentrations from the median of their upper and lower bounds. This term can be justified

547 by the trade-off in increasing concentrations between elevation of enzyme efficiency and
548 cellular burden from osmotic pressure and toxicity (*40*, *66*). Since the objective function
549 includes terms with greatly different orders of magnitude due to $\epsilon \in \{\epsilon_1, \epsilon_2\}$, it has difficulty
550 in optimized at once. Therefore, in implementation, we first solve the optimization problem
551 only for the first term, then, with the measured metabolite concentrations and $\Delta_f G'^{\circ}$ fixed
552 to the obtained solutions, and then solve the optimization problem for the second and third
553 terms.
554
555 Metabolic networks can include reversible reactions and their directions are unknown under
556 a condition of interest. By introducing binary variables representing reaction, GLEAM model
557 is finally formalized by the following mixed integer quadratic programming problem:
558

$$\min_{y\in\{\ln c,\Delta_f G'^{\circ}\},a,v,d} Z_{\mathrm{MIQP}}$$

$$= \sum_{y} \frac{1}{\#y^{\exp}} \left\{ (\boldsymbol{y}+\boldsymbol{a}-\boldsymbol{y}^{\mathbf{exp}})^{\mathrm{T}} \boldsymbol{\Sigma}_{(y)}^{-1} (\boldsymbol{y}+\boldsymbol{a}-\boldsymbol{y}^{\mathbf{exp}}) + \sum_{i} \lambda \left| \frac{(\boldsymbol{P_i})^{\mathrm{T}} \boldsymbol{a}}{\sqrt{D_{ii}}} \right| \right\}$$

$$+ \epsilon_1 \sum_{(h_1,h_2)\in H^{\mathrm{adj}}} \frac{1}{(h_2-h_1)} \sum_{i\in M^{\mathrm{unmeasured}}} \left(\ln c_{i,h_2} - \ln c_{i,h_1}\right)^2$$

$$+ \epsilon_2 \sum\nolimits_{i\in M^{\mathrm{unmeasured}}} \left(\ln c_i - \widehat{\ln c_i}\right)^2$$

$$\text{s.t.} \qquad d_j \cdot \Delta_r G_j' < 0 \quad \forall i \in M, \forall j \in N$$

$$\Delta_r G_j' = \sum_{i\in M} S_{i,j} \left(\Delta_f G_i'^{\circ} + RT \ln c_i\right) < 0 \quad \forall i \in M, \forall j \in N^{\mathrm{cell}}$$

$$\Delta_r G'_{\mathrm{GLUT}} = RT \ln \frac{[\mathrm{Glu[h]}]}{[\mathrm{Glu[b]}]}$$

$$\Delta_r G'_{\mathrm{LDH}} = RT \ln \frac{[\mathrm{H^+[b]}][\mathrm{Lac[b]}]}{[\mathrm{H^+[h]}][\mathrm{Lac[h]}]} \tag{9}$$

$$d_j \in \{-1,1\} \quad \forall j \in N^{\mathrm{rev}}$$

$$d_j \in \{1\} \quad \forall j \in N^{\mathrm{irrev_f}}$$

$$d_j \in \{-1\} \quad \forall j \in N^{\mathrm{irrev_b}}$$

$$d_j \cdot v_j > 0 \quad j \in N$$

$$\sum_{j\in N} S_{i,j} v_j = 0 \quad i \in M^{\mathrm{steady}}$$

$$lb_i \le \ln c_i \le ub_i \quad \forall i \in M$$

$$lb_i \le \ln \frac{c_{i_1}}{c_{i_2}} \le ub_i \quad \forall (i_1, i_2) \in M^{\mathrm{cofactor}}$$

559 where $v_j$ is metabolic flux through reaction $j$, $d_j = \{1, -1\}$ is a binary variable
560 representing direction of reaction $j$, and $N^{\mathrm{rev}}$ is reversible reactions. $N^{\mathrm{irrev_f}}$ and $N^{\mathrm{irrev_b}}$
561 are irreversible reactions of which the direction is fixed to forward and backward with respect
562 to the definition of metabolic network, respectively. $M^{\mathrm{steady}}$ is metabolites assumed to be
563 in steady state. To solve this mixed integer quadratic programming problem efficiently,
564 GLEAM treats it as a bilevel optimization problem, where the optimization of binary
565 variables is the upper-level problem and the optimization of continuous variables is the
566 lower-level problem:

$$\begin{aligned} \min_{d} \quad & Z_{\mathrm{MIQP}}\,(y^*, a^*, v^*, d) \\ \text{s.t.} \quad & y^*, a^*, v^* \in \arg\min_{y,a,v} Z_{\mathrm{MIQP}}(y, a, v, d) \\ & y, a, v, d \in \Omega_{\mathrm{GLEAM}} \end{aligned} \tag{10}$$

567 where $\Omega_{\mathrm{GLEAM}}$ is the solution space defined in the problem (9). In the bilevel optimization
568 problem, binary variables are optimized by a genetic algorithm, while continuous variables
569 are optimized by the interior-point method under the individuals of binary variables (Fig. S5).
570 The genetic algorithm was performed by the MATLAB function ga with termination
571 condition of FunctionTolerance = $10^{-9}$ and population size of PopulationSize = 500. The
572 lower-level quadratic programming problem was solved using Gurobi (*67*) MATLAB API
573 with dual feasibility tolerance of OptimalityTol = $10^{-9}$ and primal feasibility tolerance of
574 FeasibilityTol = $10^{-9}$. This bilevel optimization was performed 10 times from random initial
575 values, and the solution with the minimum objective function value was selected as the
576 optimal solution.
577

578 **Calculation of confidence intervals**

579 The confidence intervals of the estimation by GLEAM were calculated using parametric
580 bootstrap sampling of metabolite concentrations and $\Delta_f G'^{\circ}$. These data were first resampled
581 by adding perturbation based on the variance and residual of each metabolite concentration
582 and $\Delta_f G'^{\circ}$ in the $\Delta_r G'$ estimation by equation (9) using the experimental and database
583 values (*27*, *68*). To generate $\Delta_f G'^{\circ}$ samples reflecting their covariance, the perturbations
584 were applied after the basis of $\Delta_f G'^{\circ}$ vector was transformed by transposed matrix of the
585 eigenvectors of the variance-covariance matrix:

$$\ln c_i^{b,\mathrm{exp}} = \ln c_i^{\mathrm{exp}} + \sigma_i \delta_i^b, \ \ \forall b \in B, \tag{11}$$

$$\left(\boldsymbol{P}_{(\Delta_f \boldsymbol{G}'^{\circ})\boldsymbol{i}}\right)^{\mathrm{T}} \boldsymbol{\Delta_f G'^{o,b,\mathrm{exp}}} = \left(\boldsymbol{P}_{(\Delta_f \boldsymbol{G}'^{\circ})\boldsymbol{i}}\right)^{\mathrm{T}} \boldsymbol{\Delta_f G'^{o,\mathrm{exp}}} + \sqrt{D_{(\Delta_f G'^{o})ii}}\,\delta_i^b, \tag{12}$$

$$\boldsymbol{\Sigma^b} = \boldsymbol{\Sigma}, \tag{13}$$

$$\delta_i^b \sim \mathcal{N}(0, (sd^*)^2), \tag{14}$$

$$sd^* = \sqrt{\frac{1}{\#y^{\mathrm{exp}} - 1} \sum_{i \in \mathrm{columns}} \left( \frac{\left(\boldsymbol{P}_{(y)i}\right)^{\mathrm{T}} \boldsymbol{y}^* + \left(\boldsymbol{P}_{(y)i}\right)^{\mathrm{T}} \boldsymbol{a}^* - \left(\boldsymbol{P}_{(y)i}\right)^{\mathrm{T}} \boldsymbol{y}^{\mathrm{exp}}}{\sqrt{D_{(y)ii}}} - err^* \right)^2}, \tag{15}$$

$$err^* = \frac{1}{\#y^{\mathrm{exp}}} (\boldsymbol{y}^* + \boldsymbol{a}^* - \boldsymbol{y}^{\mathrm{exp}})^{\mathrm{T}} \boldsymbol{\Sigma}_{(y)}^{-1} (\boldsymbol{y}^* + \boldsymbol{a}^* - \boldsymbol{y}^{\mathrm{exp}}) \tag{16}$$

586 where $b$ is the indices of bootstrap samples $B$, $*$ represents the optimized values by
587 equation (9) using the experimental and database values. $\delta$ is gaussian noise generated from
588 the normal distribution with mean 0 and standard deviation $sd^*$, which represents the
589 standard deviation of metabolite concentration and $\Delta_f G'^{\circ}$ residuals in the $\Delta_r G'$ estimation

590 from the experimental and database values. Using the resampled metabolite concentrations
591 and $\Delta_f G'^{\circ}$ values, we conducted the estimation of thermodynamically consistent metabolite
592 concentrations and $\Delta_f G'^{\circ}$ in the same manner as the estimation from the experimental and
593 database values. In this optimization, the directions of reversible reactions were fixed to those
594 estimated from the experimental and database values. This resampling and optimization were
595 performed 2000 times. By applying the percentile method to the resulting 2000 sets of the
596 estimated values, we obtained the 95% confidence intervals.
597

598 **Selection of regularization parameter**

599 The regularization parameter $\lambda$ for systematic errors in GLEAM was selected by the
600 reduced chi-square ( $\chi^2_{\mathrm{red}}$ ). $\chi^2_{\mathrm{red}}$ was calculated using the estimated metabolite
601 concentrations and $\Delta_f G'^{\circ}$ from resampled values (*27*, *68*):

$$\chi^2_{\mathrm{red}} = \frac{\#y^{\mathrm{exp}} EPE}{df}, \tag{17}$$

$$EPE = \frac{1}{\#B} \sum_{b \in B} \frac{1}{\#y^{\mathrm{exp}}} \left(\boldsymbol{y}^{b*} + \boldsymbol{a}^{b*} - \boldsymbol{y}^{\mathbf{exp}}\right)^{\mathrm{T}} \boldsymbol{\Sigma}_{(y)}^{-1} \left(\boldsymbol{y}^{b*} + \boldsymbol{a}^{b*} - \boldsymbol{y}^{\mathbf{exp}}\right), \tag{18}$$

$$df = \frac{\#y^{\mathrm{exp}}}{2sd^*} (EPE - err^*) \tag{19}$$

602 where $b*$ represents the optimized values calculated from the resampled values. The model
603 is interpreted as fitting the data ideally when $\chi^2_{\mathrm{red}}$ = 1, as overfitting when $\chi^2_{\mathrm{red}}$ < 1, and
604 as poorly fitting when $\chi^2_{\mathrm{red}}$ > 1. In this study, $\chi^2_{\mathrm{red}}$ = 1.03 when $\lambda$ = 0.18, and therefore it
605 was selected as the best regularization parameter.
606

607 **Application of GLEAM to mice data**

608 We applied GLEAM to absolute quantitative metabolome data in the liver, skeletal muscle,
609 and plasma from WT and *ob*/*ob* mice (n = 5) after 0, 2, 4, 6, 8, 12, and 16 hours of fasting
610 (data file S1), which were measured in our previous studies (*8*, *69*). We used the logarithmic
611 mean and variance of the metabolites, which were successfully measured in three or more
612 samples per condition, and metabolites with two or fewer measured samples were treated as
613 unmeasured metabolites. The cofactors ATP, ADP, GTP, GDP, $NAD^+$, NADH, FAD, FADH2,
614 $NADP^+$, and NADPH were treated as unmeasured metabolites regardless of the number of
615 measured samples due to sample degradation, and instead, their ratios were constrained by
616 previous reports (Table S1). Intracellular lactate was also treated as an unmeasured
617 metabolite in the same manner as the cofactors because it might leach out of the container
618 during measurement. The upper and lower bounds for many metabolites in GLEAM were set
619 to a physiologically typical range of intracellular metabolite concentration (lower bound: $10^{-}$
620 $^{7}$ M, upper bound: $10^{-2}$ M) (*26*), while the bounds for some unmeasured metabolites were
621 individually defined based on biological knowledge (Table S1).

622

623 $\Delta_f G'^{\circ}$ data calculated by the component contribution method (*65*) were retrieved from
624 eQuilibrator database (data file S1) (*53*). We used the identical $\Delta_f G'^{\circ}$ data for both liver and
625 skeletal muscle under the condition in eQulibrator of pH = 7.2, pMg = 3.0, and ionic strength
626 = 0.15 M (*26*). We also set the condition in blood to pH = 7.4 (*70*) because $\Delta_r G'$ for MCT
627 depends on pH in the cells and blood. Temperature was input to $T$ = 310.15 K for all the
628 compartments.

629

630 In the liver, glycolysis was assumed to be dominant at the 0h-fasting state (*ad libitum* feeding)
631 while gluconeogenesis was assumed to take over after no later than 16h-fasting, both in WT
632 (*71–75*) and *ob*/*ob* mouse (*76*). At these two timepoints, the directions of reversible reactions
633 involved in glycolysis and gluconeogenesis (GPI, ALDO, TPI, GAPDH:PGK, PGAM, ENO,
634 PGM, GPD, LDH) were fixed and treated as those of the irreversible reactions in the
635 calculation of GLEAM.

636

637 Since the reaction rates are sufficiently faster than the temporal changes in metabolite and
638 enzyme levels during starvation, our metabolic model was assumed to be in a pseudo-steady
639 state at each measured time point. This assumption leads to mass balance equilibrium for the
640 intermediate metabolites (G6P, F6P, F1,6BP, DHAP, GAP, 3PG, 2PG, PEP, Pyruvate, AcCoA,
641 Cit, Isocit, AKG, SucCoA, Suc, Fum, Mal, OAA) within the metabolic network.

642

643 **Derivation of FCC**

644 We derived flux control coefficients (FCCs) within glycolysis (Fig. 3A), gluconeogenesis
645 (Fig. 3B), and the TCA cycle (Fig. 3C) from the direct binding modular rate law (*48*), which
646 is equivalent to the reversible Michaelis-Menten kinetics (*77*) for simple reversible uni-uni
647 reactions, using theorems of Metabolic Control Analysis (MCA) (*36*, *47*). In the direct
648 binding modular rate law, flux can be described by the effect of the maximal rate, the
649 thermodynamics, and the saturation of substrate (*49*):

$$v = Ek_{\mathrm{cat}}^{+}\eta_{\mathrm{rev}}\eta_{\mathrm{sat,s}}, \tag{20}$$

$$\eta_{\mathrm{rev}} = 1 - \exp\left(\frac{\Delta_r G'}{RT}\right), \tag{21}$$

$$\eta_{\mathrm{sat,s}} = \frac{\prod_{i\in M^{\mathrm{s}}}\left(\frac{c_i}{K_{\mathrm{m},i}}\right)^{|S_i|}}{1 + \prod_{i\in M^{\mathrm{s}}}\left(\frac{c_i}{K_{\mathrm{m},i}}\right)^{|S_i|} + \prod_{i\in M^{\mathrm{p}}}\left(\frac{c_i}{K_{\mathrm{m},i}}\right)^{|S_i|}} \tag{22}$$

where $M^{\mathrm{s}}$ is substrates, $M^{\mathrm{p}}$ is products. From equation (20), we calculated the elasticity of substrate $\epsilon_{\mathrm{s},i}^{v}$ and product $\epsilon_{\mathrm{p},i}^{v}$:

$$\epsilon_{\mathrm{s},i}^{v} = \frac{\partial v}{\partial c_i}\frac{c_i}{v} = |S_i|\left(\eta_{\mathrm{rev}}^{-1} - \eta_{\mathrm{sat,s}}\right), \tag{23}$$

$$\epsilon_{\mathrm{p},i}^{v} = \frac{\partial v}{\partial c_i}\frac{c_{\mathrm{i}}}{v} = |S_i|\left(1 - \eta_{\mathrm{rev}}^{-1} - \eta_{\mathrm{sat,p}}\right), \tag{24}$$

$$\eta_{\mathrm{sat,p}} = \frac{\prod_{i\in M^{\mathrm{p}}}\left(\frac{c_i}{K_{\mathrm{m},i}}\right)^{|S_i|}}{1 + \prod_{i\in M^{\mathrm{s}}}\left(\frac{c_i}{K_{\mathrm{m},i}}\right)^{|S_i|} + \prod_{i\in M^{\mathrm{p}}}\left(\frac{c_i}{K_{\mathrm{m},i}}\right)^{|S_i|}}. \tag{25}$$

The stoichiometric matrices of the pathways we analyzed here are full rank, and each of their null spaces is one-dimensional, which means the degree of freedom of steady-state flux is one. For these pathways, the following equations (26) and (27) hold from the connectivity theorem and the summation theorem in MCA, respectively (*50*):

$$\mathbf{C}_{\mathbf{v}}^{\mathbf{J}}\boldsymbol{\epsilon}_{\mathbf{c}}^{\mathbf{v}} = \mathbf{0}, \tag{26}$$

$$\sum_{j} C_{v_j}^{J} = 1, \tag{27}$$

$$\mathbf{C_v^J} = \begin{pmatrix} C_{v_1}^J & \cdots & C_{v_n}^J \\ \vdots & \ddots & \vdots \\ C_{v_1}^J & \cdots & C_{v_n}^J \end{pmatrix}, \tag{28}$$

$$\boldsymbol{\epsilon}_\mathbf{c}^\mathbf{v} = \begin{pmatrix} \epsilon_{c_1}^{v_1} & \cdots & \epsilon_{c_k}^{v_1} \\ \vdots & \ddots & \vdots \\ \epsilon_{c_1}^{v_n} & \cdots & \epsilon_{c_k}^{v_n} \end{pmatrix} \tag{29}$$

where $\epsilon_c^v = \{\epsilon_s^v, \epsilon_p^v\}$. Integrating equations (23), (24), (26) and (27), we obtained FCC as:

$$C_{v_l}^J = \frac{\alpha_l}{\sum_j \alpha_j}, \tag{30}$$

where $\alpha$ for GAPDH:PGK in glycolysis is described as

$$\alpha = \prod_{j=0}^{\text{ALDO}} \left(-\epsilon_\text{p}^{v_j}\right)\left(\epsilon_\text{s}^{v_\text{TPI}} - \epsilon_\text{p}^{v_\text{TPI}}\right) \prod_{j=l+1}^{n+1} \epsilon_\text{s}^{v_j}, \tag{31}$$

$\alpha$ for downstream reactions of GAPDH:PGK in glycolysis is described as

$$\alpha = \prod_{j=0}^{\text{ALDO}} \left(-\epsilon_\text{p}^{v_j}\right)\left(\epsilon_\text{s}^{v_\text{TPI}} - \epsilon_\text{p}^{v_\text{TPI}}\right) \prod_{j=\text{GAPDH:PGK}}^{l-1} \left(-\epsilon_\text{p}^{v_l}\right) \prod_{j=l+1}^{n+1} \epsilon_\text{s}^{v_j}, \tag{32}$$

$\alpha$ for ALDO in gluconeogenesis is described as

$$\alpha = \prod_{j=0}^{\text{GAPDH:PGK}} \left(-\epsilon_\text{p}^{v_j}\right)\left(\epsilon_\text{s}^{v_\text{TPI}} - \epsilon_\text{p}^{v_\text{TPI}}\right) \prod_{j=l+1}^{n+1} \epsilon_\text{s}^{v_j}, \tag{33}$$

$\alpha$ for downstream reactions of ALDO in gluconeogenesis is described as

$$\alpha = \prod_{j=0}^{\text{GAPDH:PGK}} \left(-\epsilon_\text{p}^{v_j}\right)\left(\epsilon_\text{s}^{v_\text{TPI}} - \epsilon_\text{p}^{v_\text{TPI}}\right) \prod_{j=\text{ALDO}}^{l-1} \left(-\epsilon_\text{p}^{v_j}\right) \prod_{j=l+1}^{n+1} \epsilon_\text{s}^{v_j}, \tag{34}$$

$\alpha$ for other reactions is described as

$$\alpha_l = \prod_{j=0}^{l-1}\left(-\epsilon_{\mathrm{p}}^{v_j}\right)\prod_{j=l+1}^{n+1}\epsilon_{\mathrm{s}}^{v_j}. \tag{35}$$

Note that reaction indices $j \in \{1, \ldots, N\}$ are denoted such that 1 represents the most upstream reaction and N represents the most downstream reaction in the pathway, and $\epsilon_{\mathrm{s}}^{v_0} = \epsilon_{\mathrm{p}}^{v_0} = \epsilon_{\mathrm{s}}^{v_{n+1}} = \epsilon_{\mathrm{p}}^{v_{n+1}} = 1$.

**Metabolite concentrations and $\Delta_f G'^{\circ}$ values used in FCC calculation**

We calculated FCC under arbitrary $\Delta_r G'$ landscapes as well as under the hepatic one. For both conditions, we used $\Delta_f G'^{\circ}$ values sampled for confidence interval calculation in GLEAM. To generate the hepatic $\Delta_r G'$ landscapes, we used metabolite concentrations sampled in the confidence interval calculation. To generate arbitrary $\Delta_r G'$ landscapes, logarithmic metabolite concentrations were uniformly sampled from the physiologically reasonable solution space $\Omega_{\ln c}$:

$$\Omega_{\ln c} = \left\{ \ln c \;\middle|\; \begin{array}{c} \Delta_r G_j' < 0 \\ lb_i \leq \ln c_i \leq ub_i \\ lb_i = ub_i = \ln c_i^{\mathrm{blood}} \quad i \in M^{\mathrm{blood}} \end{array} \right\} \tag{36}$$

where $M^{\mathrm{blood}}$ represents blood metabolites. The upper and lower bounds of metabolite concentrations were the same as those used in GLEAM (Table S1). This sampling was performed 20 times for each $\Delta_f G'^{\circ}$ set using MATLAB function polySampler in the Volume-and-Sampling package (*78*). Thus, we obtained 2000 × 20 = 40000 arbitrary $\Delta_r G'$ landscapes in total.

678

679 **$K_{\mathrm{m}}$ values used in FCC calculation**

680 In FCC calculation, we sampled Michaelis-Menten constants $K_{\mathrm{m}}$ for each $\Delta_r G'$ landscape
681 to calculate reaction saturation level. To sample $K_{\mathrm{m}}$, we first retrieved $K_{\mathrm{m}}$ and the turnover
682 number, $k_{\mathrm{cat}} \in \{k_{\mathrm{cat}}^{+}, k_{\mathrm{cat}}^{-}\}$ values for enzymes of *Mus musculus*, *Rattus norvegicus*, *Homo*
683 *sapiens*, *Bos taurus*, *Sus scrofa*, *Canis lupus familiaris*, and *Mammalia* (*79*) from BRENDA
684 database (*79*). For $K_{\mathrm{m}}$ and $k_{\mathrm{cat}}$ values from three or more data without reports of mutant
685 enzymes, we calculated their logarithmic means and standard deviations. For $K_{\mathrm{m}}$ and $k_{\mathrm{cat}}$
686 from fewer than three data, we set the logarithmic mean of $k_{\mathrm{cat}}$ (/s) to 1 with a standard
687 deviation of 1.5, and the logarithmic mean of $K_{\mathrm{m}}$ (mM) to −1 with a standard deviation of
688 1 (*80*). With the means and standard deviations of $K_{\mathrm{m}}$ and $k_{\mathrm{cat}}$, we uniformly sampled
689 logarithmic $K_{\mathrm{m}}$, $k_{\mathrm{cat}}$ values for each enzyme from the solution space $\Omega_{\mathrm{KP}}$:

$$\Omega_{\mathrm{KP},j} = \left\{ \begin{pmatrix} \log K_{\mathrm{m}} \\ \log k_{\mathrm{cat}} \end{pmatrix} \middle| \begin{array}{c} \log \mu^{K_{\mathrm{m},i,j}} - 2\sigma^{K_{\mathrm{m},i,j}} \leq \log K_{\mathrm{m},i,j} \leq \log \mu^{K_{\mathrm{m},i,j}} + 2\sigma^{K_{\mathrm{m},i,j}} \\ \log \mu^{k_{\mathrm{cat},j}} - 2\sigma^{k_{\mathrm{cat},j}} \leq \log k_{\mathrm{cat},j} \leq \log \mu^{k_{\mathrm{cat},j}} + 2\sigma^{k_{\mathrm{cat},j}} \\ \log k_{\mathrm{cat},j}^{+} - \log k_{\mathrm{cat},j}^{-} - \sum_{i \in M^{\mathrm{s}}} \log K_{\mathrm{m},i,j}^{|S_{i,j}|} + \sum_{i \in M^{\mathrm{p}}} \log K_{\mathrm{m},i,j}^{|S_{i,j}|} = \log K_{\mathrm{eq},j} \\ K_{\mathrm{eq},j} = \exp\left( -\frac{1}{RT} \sum_{i \in M} S_{i,j} \Delta_f G_i'^{\circ} \right) \end{array} \right\}, \quad (37)$$

$\forall i \in M, \forall j \in N$

690 where $\mu$ is mean, $\sigma$ is standard deviation, and $K_{\mathrm{eq}}$ is equilibrium constant. The third
691 constraint equation reflects the Haldane relationship (*80*). These samplings were performed
692 20 times for each $\Delta_r G'$ landscape using MATLAB function polySampler in the Volume-

693 and-Sampling package (*78*). Thus, we finally calculated FCC under the arbitrary and hepatic
694 $\Delta_r G'$ landscapes with 20 × 20 × 2000 = 800000 and 20 × 2000 = 40000 sets of metabolite
695 concentrations, $\Delta_f G'^{\circ}$ and $K_{\mathrm{m}}$ values, respectively.
696
697 **Definitions of EC and total EC**
698 By solving the equation of the direct binding modular rate law with respect to enzyme amount,
699 we can obtain enzyme demand needed to carry a certain flux:

$$E = \frac{v}{k_{\mathrm{cat}}^{+}} \eta_{\mathrm{rev}}^{-1} \eta_{\mathrm{sat,s}}^{-1}. \tag{39}$$

700 With this equation, we defined Enzyme Cost (EC) as the product of the enzyme demand and
701 the enzyme molecular weight *w*:

$$\mathrm{EC} = wE. \tag{40}$$

702 The enzyme molecular weights were retrieved from the UniProt database (*8*, *69*). We also
703 defined pathway's total EC as the sum of ECs in the pathway:

$$\text{total EC} = \sum_{j \in N^{\mathrm{pathway}}} \mathrm{EC}_j \tag{41}$$

704 where $N^{\mathrm{pathway}}$ is reactions included in the pathway. We calculated ECs in glycolysis (Fig.
705 3A), gluconeogenesis (Fig. 3B), and the TCA cycle (Fig. 3C), which were the same as those
706 used in FCC calculations, under the hepatic $\Delta_r G'$ landscape using metabolite concentrations
707 and $\Delta_f G'^{\circ}$ values sampled for confidence interval calculation in GLEAM, and geometric
708 mean of $K_{\mathrm{m}}$ values from the BRENDA database (*51*) obtained in FCC calculation (data file
709 S4). For $K_{\mathrm{m}}$ with fewer than three data found in the BRENDA, we set their $c/K_{\mathrm{m}}$ values

710 to the geometric mean of the pathway. $k_{\mathrm{cat}}^{+}$ values were assumed to be the same within a
711 pathway, and their effect can be ignored in this study because we only focused on the relative
712 values of EC.
713
714 **Minimization of total EC**
715 Since EC is dependent on metabolite concentrations, we defined Enzyme Cost Minimum
716 (ECM) as a theoretical condition where total EC is minimized with metabolite concentrations.
717 We obtained ECM by solving the following non-linear optimization problem (*26*):

$$
\begin{aligned}
\min_{\ln c} \quad & \text{total EC} = \sum_{j \in N^{\mathrm{pathway}}} \mathrm{EC}_j \\
\text{s.t.} \quad & \mathrm{EC}_j = wv\eta_{\mathrm{rev},j}^{-1}\eta_{\mathrm{sat,s},j}^{-1}, \ \ j \in N \\
& \eta_{\mathrm{rev},j} = 1 - \exp\left(\frac{\Delta_r G_j'}{RT}\right) \\
& \eta_{\mathrm{sat,s},j} = \frac{\prod_{i \in M^{\mathrm{s}}} \left(\frac{c_i}{K_{\mathrm{m},i,j}}\right)^{|S_{i,j}|}}{1 + \prod_{i \in M^{\mathrm{s}}} \left(\frac{c_i}{K_{\mathrm{m},i,j}}\right)^{|S_{i,j}|} + \prod_{i \in M^{\mathrm{p}}} \left(\frac{c_i}{K_{\mathrm{m},i,j}}\right)^{|S_{i,j}|}} \\
& \Delta_r G_j' = \sum_{i \in M} S_{i,j}\left(\Delta_f G_i'^{\circ,\mathrm{liver}} + RT \ln c_i\right) < 0, \ \ j \in N \\
& lb_i \le \ln c_i \le ub_i, \ \ i \in M \\
& lb_i = ub_i = \ln c_i^{\mathrm{blood}}, \ \ i \in M^{\mathrm{blood}} \\
& lb_i = ub_i = \ln c_i^{\mathrm{liver}}, \ \ i \in M^{\mathrm{terminal}} \\
& \ln \frac{c_{i_1}}{c_{i_2}} = \left(\ln \frac{c_{i_1}}{c_{i_2}}\right)^{\mathrm{liver}}, \ \ \forall (i_1, i_2) \in M^{\mathrm{cofactor}}.
\end{aligned}
\tag{42}
$$

718 *w* and *v* are normalized by the minimum molecular weight and flux, respectively. The relative
719 flux values for a pathway we analyzed were unique because the degree of freedom of these
720 pathways' steady flux is 1. $M^{\mathrm{blood}}$ represents blood metabolites, and $M^{\mathrm{terminal}}$ represents
721 intracellular metabolites at the termini of each pathway: Glucose and Pyr for glycolysis and
722 gluconeogenesis, and AcCoA, OAA, and Mal for the TCA cycle. By fixing these
723 concentrations and cofactor ratios to those in mouse liver, the total Gibbs free energy change
724 across the entire pathway in ECM is consistent with that in the mouse liver. ECM was
725 calculated by MATLAB function fmincon with termination tolerance on the first-order
726 optimality of OptimalityTolerance = $10^{-7}$, tolerance on the constraint violation of
727 ConstraintTolerance = $10^{-9}$, maximum number of function evaluations of
728 MaxFunctionEvaluations = 1000000, and maximum number of iterations of MaxIterations =
729 100000. The optimization was performed 100 times for a single problem, and the solution
730 minimizing the objective function was selected as ECM.
731

732 **Calculation of MEG**

733 To quantify the efficiency of metabolic switching in terms of metabolite concentration
734 changes, we defined the Metabolite Equilibrium Gap (MEG) as the minimum concentration
735 changes required to reverse the direction of metabolism:

$$\begin{aligned} &\mathrm{MEG} = \exp A \\ &A = \min_{\ln c} \sqrt{\frac{1}{\#M}\sum_{i\in M}\left(\ln c_i - \ln c_i^{\mathrm{sys}}\right)^2} \\ \text{s.t.}\quad &\Delta_r G_j' = \sum_{i\in M} S_{i,j}\left(\Delta_f G_i'^{\circ} + RT\ln c_i\right) = 0, \quad j \in N^{\mathrm{shift}} \\ &\Delta_r G_j' = \sum_{i\in M} S_{i,j}\left(\Delta_f G_i'^{\circ} + RT\ln c_i\right) < 0, \quad j \in N \notin N^{\mathrm{shift}} \\ &b_i \le \ln c_i \le ub_i, \ \ j \in M \end{aligned} \tag{43}$$

where sys represents a value in a target system corresponding to the liver or ECM in this study. $N^{\mathrm{shift}}$ is the reactions that must proceed in the reverse direction when switching metabolisms; it includes reversible reactions in glycolysis and gluconeogenesis, and all reactions in the TCA cycle. $\Delta_f G'^{\circ}$ values used in MEG calculation were the same as those in the liver (and also the same as those in ECM). MEG was calculated using Gurobi (*67*) MATLAB API with dual feasibility tolerance of OptimalityTol = $10^{-9}$ and primal feasibility tolerance of FeasibilityTol = $10^{-9}$.

**Implementation and statistical analysis**

Statistical tests, optimizations, computational samplings, and calculations of $\Delta_r G'$, FCC, and EC were performed using MATLAB 2021b (The MathWorks Inc.) and Gurobi (version 10.0.3) (*67*). Database handlings were performed using Python (version 3.10. All details of statistical tests are described in the Results section. The MATLAB package Plot Groups of Stacked Bars (*82*) was used to create the figures.

**Supplementary Materials**

Figs. S1 to S5

Tables S1 to S2

Data files S1 to S5

References (*81*) to (*91*)

## References


1. M. C. Scrutton, M. F. Utter, The Regulation of Glycolysis and Gluconeogenesis in Animal Tissues. *Annu. Rev. Biochem.* **37**, 249–302 (1968).

2. D. L. Rothman, I. Magnusson, L. D. Katz, R. G. Shulman, G. I. Shulman, Quantitation of Hepatic Glycogenolysis And Gluconeogenesis in Fasting Humans With $^{13}$C NMR. *Science* **254**, 573–576 (1991).

3. R. C. Nordlie, J. D. Foster, A. J. Lange, Regulation of glucose production by the liver. *Annu. Rev. Nutr.* **19**, 379–406 (1999).

4. M. C. Moore, K. C. Coate, J. J. Winnick, Z. An, A. D. Cherrington, Regulation of hepatic glucose uptake and storage in vivo. *Adv. Nutr.* **3**, 286–294 (2012).

5. H.-S. Han, G. Kang, J. S. Kim, B. H. Choi, S.-H. Koo, Regulation of glucose metabolism from a liver-centric perspective. *Exp. Mol. Med.* **48**, e218 (2016).

6. J. Katz, J. A. Tayek, Gluconeogenesis and the Cori cycle in 12-, 20-, and 40-h-fasted humans. *American Journal of Physiology-Endocrinology and Metabolism* **275**, E537–E542 (1998).

7. R. Egami, T. Kokaji, A. Hatano, K. Yugi, M. Eto, K. Morita, S. Ohno, M. Fujii, K.-I. Hironaka, S. Uematsu, A. Terakawa, Y. Bai, Y. Pan, T. Tsuchiya, H. Ozaki, H. Inoue, S. Uda, H. Kubota, Y. Suzuki, M. Matsumoto, K. I. Nakayama, A. Hirayama, T. Soga, S. Kuroda, Trans-omic analysis reveals obesity-associated dysregulation of inter-organ metabolic cycles between the liver and skeletal muscle. *iScience* **24**, 102217 (2021).

8. K. Morita, A. Hatano, T. Kokaji, H. Sugimoto, T. Tsuchiya, H. Ozaki, R. Egami, D. Li, A. Terakawa, S. Ohno, H. Inoue, Y. Inaba, Y. Suzuki, M. Matsumoto, M. Takahashi, Y. Izumi, T. Bamba, A. Hirayama, T. Soga, S. Kuroda, Structural robustness and temporal vulnerability of the starvation-responsive metabolic network in healthy and obese mouse liver. *Sci. Signal.* **18**, eads2547 (2025).

9. V. T. Samuel, G. I. Shulman, The pathogenesis of insulin resistance: integrating signaling pathways and substrate flux. *J. Clin. Invest.* **126**, 12–22 (2016).

10. J. H. Stern, G. I. Smith, S. Chen, R. H. Unger, S. Klein, P. E. Scherer, Obesity dysregulates fasting-induced changes in glucagon secretion. *J. Endocrinol.* **243**, 149–160 (2019).

11. B. Stocks, A. Gonzalez-Franquesa, M. L. Borg, M. Björnholm, L. Niu, J. R. Zierath, A. S. Deshmukh, Integrated Liver and Plasma Proteomics in Obese Mice Reveals Complex Metabolic Regulation. *Mol. Cell. Proteomics* **21**, 100207 (2022).

12. Y. Bai, K. Morita, T. Kokaji, A. Hatano, S. Ohno, R. Egami, Y. Pan, D. Li, K. Yugi, S. Uematsu, H. Inoue, Y. Inaba, Y. Suzuki, M. Matsumoto, M. Takahashi, Y. Izumi, T. Bamba, A. Hirayama, T. Soga, S. Kuroda, Trans-omic analysis reveals opposite metabolic dysregulation between feeding and fasting in liver associated with obesity. *iScience* **27**, 109121 (2024).

13. I. Magnusson, D. L. Rothman, L. D. Katz, R. G. Shulman, G. I. Shulman, Increased rate of gluconeogenesis in type II diabetes mellitus. A 13C nuclear magnetic resonance study. *J. Clin. Invest.* **90**, 1323–1327 (1992).

14. R. S. Hundal, M. Krssak, S. Dufour, D. Laurent, V. Lebon, V. Chandramouli, S. E. Inzucchi, W. C. Schumann, K. F. Petersen, B. R. Landau, G. I. Shulman, Mechanism by which metformin reduces glucose production in type 2 diabetes. *Diabetes* **49**, 2063–2069 (2000).

15. A. Wajngot, V. Chandramouli, W. C. Schumann, K. Ekberg, P. K. Jones, S. Efendic, B. R. Landau, Quantitative contributions of gluconeogenesis to glucose production during fasting in type 2 diabetes mellitus. *Metabolism* **50**, 47–52 (2001).

16. K. F. Petersen, T. B. Price, R. Bergeron, Regulation of Net Hepatic Glycogenolysis and Gluconeogenesis during Exercise: Impact of Type 1 Diabetes. *J. Clin. Endocrinol. Metab.* **89**, 4656–4664 (2004).

17. M. C. Petersen, D. F. Vatner, G. I. Shulman, Regulation of hepatic glucose metabolism in health and disease. *Nat. Rev. Endocrinol.* **13**, 572–587 (2017).

18. T. K. Schramm, G. H. Gislason, L. Køber, S. Rasmussen, J. N. Rasmussen, S. Z. Abildstrøm, M. L. Hansen, F. Folke, P. Buch, M. Madsen, A. Vaag, C. Torp-Pedersen, Diabetes Patients Requiring Glucose-Lowering Therapy and Nondiabetics With a Prior Myocardial Infarction Carry the Same Cardiovascular Risk. *Circulation* **117**, 1945–1954 (2008).

19. E. A. Spencer, K. L. Pirie, R. J. Stevens, V. Beral, A. Brown, B. Liu, J. Green, G. K. Reeves, Diabetes and modifiable risk factors for cardiovascular disease: the prospective Million Women Study. *Eur. J. Epidemiol.* **23**, 793–799 (2008).

20. S. Gancheva, T. Jelenik, E. Álvarez-Hernández, M. Roden, Interorgan metabolic crosstalk in human insulin resistance. *Physiol. Rev.* **98**, 1371–1415 (2018).

21. T. M. Annesley, Ion suppression in mass spectrometry. *Clin. Chem.* **49**, 1041–1044 (2003).

22. M. R. Mashego, L. Wu, J. C. Van Dam, C. Ras, J. L. Vinke, W. A. Van Winden, W. M. Van Gulik, J. J. Heijnen, MIRACLE: mass isotopomer ratio analysis of U-13C-labeled extracts. A new method for accurate quantification of changes in concentrations of intracellular metabolites. *Biotechnol. Bioeng.* **85**, 620–628 (2004).

826 23. M. Sugimoto, A. Hirayama, M. Robert, S. Abe, T. Soga, M. Tomita, Prediction of
827 metabolite identity from accurate mass, migration time prediction and isotopic pattern
828 information in CE-TOFMS data. *Electrophoresis* **31**, 2311–2318 (2010).

829 24. B. D. Bennett, E. H. Kimball, M. Gao, R. Osterhout, S. J. Van Dien, J. D. Rabinowitz,
830 Absolute metabolite concentrations and implied enzyme active site occupancy in
831 Escherichia coli. *Nat. Chem. Biol.* **5**, 593–599 (2009).

832 25. A. B. Canelas, C. Ras, A. ten Pierick, W. M. van Gulik, J. J. Heijnen, An in vivo data-
833 driven framework for classification and quantification of enzyme kinetics and
834 determination of apparent thermodynamic data. *Metab. Eng.* **13**, 294–306 (2011).

835 26. J. O. Park, S. A. Rubin, Y. F. Xu, D. Amador-Noguez, J. Fan, T. Shlomi, J. D. Rabinowitz,
836 Metabolite concentrations, fluxes and free energies imply efficient enzyme usage. *Nat.*
837 *Chem. Biol.* **12**, 482–489 (2016).

838 27. B. Niebel, S. Leupold, M. Heinemann, An upper limit on Gibbs energy dissipation
839 governs cellular metabolism. *Nature Metabolism* **1**, 125–132 (2019).

840 28. M. L. Mavrovouniotis, Identification of localized and distributed bottlenecks in
841 metabolic pathways. *Proc. Int. Conf. Intell. Syst. Mol. Biol.* **1**, 275–283 (1993).

842 29. C. S. Henry, M. D. Jankowski, L. J. Broadbelt, V. Hatzimanikatis, Genome-Scale
843 Thermodynamic Analysis of Escherichia coli Metabolism. *Biophys. J.* **90**, 1453–1461
844 (2006).

845 30. A. M. Feist, C. S. Henry, J. L. Reed, M. Krummenacker, A. R. Joyce, P. D. Karp, L. J.
846 Broadbelt, V. Hatzimanikatis, B. Ø. Palsson, A genome-scale metabolic reconstruction
847 for Escherichia coli K-12 MG1655 that accounts for 1260 ORFs and thermodynamic
848 information. *Mol. Syst. Biol.* **3**, 121 (2007).

849 31. C. S. Henry, L. J. Broadbelt, V. Hatzimanikatis, Thermodynamics-based metabolic flux
850 analysis. *Biophys. J.* **92**, 1792–1805 (2007).

851 32. K. C. Soh, V. Hatzimanikatis, Network thermodynamics in the post-genomic era. *Curr.*
852 *Opin. Microbiol.* **13**, 350–357 (2010).

853 33. J. J. Hamilton, V. Dwivedi, J. L. Reed, Quantitative assessment of thermodynamic
854 constraints on the solution space of genome-scale metabolic models. *Biophys. J.* **105**,
855 512–522 (2013).

856 34. L. Seep, Z. Razaghi-Moghadam, Z. Nikoloski, Reaction lumping in metabolic networks
857 for application with thermodynamic metabolic flux analysis. *Sci. Rep.* **11**, 8544 (2021).

35. M. Janasch, N. Crang, J. Asplund-Samuelsson, E. Sporre, M. Bruch, A. Gynnå, M. Jahn, E. P. Hudson, Thermodynamic limitations of PHB production from formate and fructose in Cupriavidus necator. *Metab. Eng.* **73**, 256–269 (2022).

36. H. Kacser, J. A. Burns, The control of flux. *Symp. Soc. Exp. Biol.* **27**, 65–104 (1973).

37. Z. Dai, J. W. Locasale, Thermodynamic constraints on the regulation of metabolic fluxes. *J. Biol. Chem.* **293**, 19725–19739 (2018).

38. D. D. van Niekerk, E. Rust, F. Bruggeman, H. V. Westerhoff, J. L. Snoep, Is distance from equilibrium a good indicator for a reaction's flux control? *Biosystems.* **232**, 104988 (2023).

39. A. Flamholz, E. Noor, A. Bar-Even, W. Liebermeister, R. Milo, Glycolytic strategy as a tradeoff between energy yield and protein cost. *Proceedings of the National Academy of Sciences* **110**, 10039–10044 (2013).

40. N. Tepper, E. Noor, D. Amador-Noguez, H. S. Haraldsdóttir, R. Milo, J. Rabinowitz, W. Liebermeister, T. Shlomi, Steady-State Metabolite Concentrations Reflect a Balance between Maximizing Enzyme Efficiency and Minimizing Total Metabolite Load. *PLoS One* **8**, e75370 (2013).

41. E. Noor, A. Bar-Even, A. Flamholz, E. Reznik, W. Liebermeister, R. Milo, Pathway Thermodynamics Highlights Kinetic Obstacles in Central Metabolism. *PLoS Comput. Biol.* **10** (2014).

42. E. Noor, A. Flamholz, A. Bar-Even, D. Davidi, R. Milo, W. Liebermeister, The Protein Cost of Metabolic Fluxes: Prediction from Enzymatic Rate Laws and Cost Minimization. *PLoS Comput. Biol.* **12**, e1005167 (2016).

43. T. Soga, Y. Ohashi, Y. Ueno, H. Naraoka, M. Tomita, T. Nishioka, Quantitative metabolome analysis using capillary electrophoresis mass spectrometry. *J. Proteome Res.* **2**, 488–494 (2003).

44. T. Soga, T. Ishikawa, S. Igarashi, K. Sugawara, Y. Kakazu, M. Tomita, Analysis of nucleotides by pressure-assisted capillary electrophoresis-mass spectrometry using silanol mask technique. *J. Chromatogr. A* **1159**, 125–133 (2007).

45. A. M. Ingalls, M. M. Dickie, G. D. Snell, Obese, a new mutation in the house mouse. *J. Hered.* **41**, 317–318 (1950).

46. P. Lindström, The physiology of obese-hyperglycemic mice [ob/ob mice]. *ScientificWorldJournal* **7**, 666–685 (2007).

47. R. Heinrich, T. A. Rapoport, A linear steady-state treatment of enzymatic chains. General properties, control and effector strength. *Eur. J. Biochem.* **42**, 89–95 (1974).

892 48. W. Liebermeister, J. Uhlendorf, E. Klipp, Modular rate laws for enzymatic reactions:
893 thermodynamics, elasticities and implementation. *Bioinformatics* **26**, 1528–1534 (2010).

894 49. E. Noor, A. Flamholz, W. Liebermeister, A. Bar-Even, R. Milo, A note on the kinetics of
895 enzyme action: A decomposition that highlights thermodynamic effects. *FEBS Lett.* **587**,
896 2772–2777 (2013).

897 50. J. H. Hofmeyr, A. Cornish-Bowden, Co-response analysis: a new experimental strategy
898 for metabolic control analysis. *J. Theor. Biol.* **182**, 371–380 (1996).

899 51. A. Chang, L. Jeske, S. Ulbrich, J. Hofmann, J. Koblitz, I. Schomburg, M. Neumann-
900 Schaal, D. Jahn, D. Schomburg, BRENDA, the ELIXIR core data resource in 2021: new
901 developments and updates. *Nucleic Acids Res.* **49**, D498–D508 (2021).

902 52. R. Schuetz, N. Zamboni, M. Zampieri, M. Heinemann, U. Sauer, Multidimensional
903 Optimality of Microbial Metabolism. *Science* **336**, 601–604 (2012).

904 53. M. E. Beber, M. G. Gollub, D. Mozaffari, K. M. Shebek, A. I. Flamholz, R. Milo, E.
905 Noor, eQuilibrator 3.0: a database solution for thermodynamic constant estimation.
906 *Nucleic Acids Res.* **50**, D603–D609 (2022).

907 54. L. B. Tanner, A. G. Goglia, M. H. Wei, T. Sehgal, L. R. Parsons, J. O. Park, E. White, J.
908 E. Toettcher, J. D. Rabinowitz, Four key steps control glycolytic flux in mammalian cells.
909 *Cell Syst.* **7**, 49-62.e8 (2018).

910 55. A. K. Groen, C. W. van Roermund, R. C. Vervoorn, J. M. Tager, Control of
911 gluconeogenesis in rat liver cells. Flux control coefficients of the enzymes in the
912 gluconeogenic pathway in the absence and presence of glucagon. *Biochem. J* **237**, 379–
913 389 (1986).

914 56. M. Rigoulet, X. M. Leverve, P. J. Plomp, A. J. Meijer, Stimulation by glucose of
915 gluconeogenesis in hepatocytes isolated from starved rats. *Biochem. J.* **245**, 661–668
916 (1987).

917 57. M. Milani, A. Pesce, M. Bolognesi, A. Bocedi, P. Ascenzi, Substrate channeling:
918 Molecular bases. *Biochem. Mol. Biol. Educ.* **31**, 228–233 (2003).

919 58. A. Datta, J. M. Merz, H. O. Spivey, Substrate channeling of oxalacetate in solid-state
920 complexes of malate dehydrogenase and citrate synthase. *J. Biol. Chem.* **260**, 15008–
921 15012 (1985).

922 59. F. Wu, S. Minteer, Krebs cycle metabolon: structural evidence of substrate channeling
923 revealed by cross-linking and mass spectrometry. *Angew. Chem. Int. Ed Engl.* **54**, 1851–
924 1854 (2015).

60. L. E. Anderson, I. M. Goldhaber-Gordon, D. Li, X. Y. Tang, M. Xiang, N. Prakash, Enzyme-enzyme interaction in the chloroplast: glyceraldehyde-3-phosphate dehydrogenase, triose phosphate isomerase and aldolase. *Planta* **196**, 245–255 (1995).

61. D. Araiza-Olivera, N. Chiquete-Felix, M. Rosas-Lemus, J. G. Sampedro, A. Peña, A. Mujica, S. Uribe-Carvajal, A glycolytic metabolon in Saccharomyces cerevisiae is stabilized by F-actin. *FEBS J.* **280**, 3887–3905 (2013).

62. A. Bordbar, A. M. Feist, R. Usaite-Black, J. Woodcock, B. O. Palsson, I. Famili, A multi-tissue type genome-scale metabolic network for analysis of whole-body systems physiology. *BMC Syst. Biol.* **5** (2011).

63. A. H. Lancha Jr, M. B. Recco, R. Curi, Pyruvate carboxylase activity in the heart and skeletal muscles of the rat. Evidence for a stimulating effect of exercise. *Biochem. Mol. Biol. Int.* **32**, 483–489 (1994).

64. A. D. Minet, M. Gaster, Pyruvate carboxylase is expressed in human skeletal muscle. *Biochem. Biophys. Res. Commun.* **402**, 196–197 (2010).

65. E. Noor, H. S. Haraldsdóttir, R. Milo, R. M. T. Fleming, Consistent Estimation of Gibbs Energy Using Component Contributions. *PLoS Comput. Biol.* **9** (2013).

66. S. Schuster, R. Heinrich, Minimization of intermediate concentrations as a suggested optimality principle for biochemical networks: I. Theoretical analysis. *J. Math. Biol.* **29**, 425–442 (1991).

67. L. L. C. Gurobi Optimization, Gurobi Optimizer Reference Manual (2024). https://www.gurobi.com/.

68. T. Hastie, R. Tibshirani, J. Friedman, *The Elements of Statistical Learning: Data Mining, Inference, and Prediction, Second Edition* (Springer, New York, NY, ed. 2, 2009)*Springer series in statistics*.

69. D. Li, K. Morita, T. Kokaji, A. Hatano, A. Hirayama, T. Soga, Y. Suzuki, M. Matsumoto, T. Tsuchiya, H. Ozaki, S. Ohno, H. Inoue, Y. Inaba, H. Sugimoto, Y. Pan, S. Kuroda, Global loss of responsiveness in key regulator metabolites and elevated enzyme proteins as metabolic dysregulation in skeletal muscle and liver of obese mice during starvation, *bioRxiv* (2025)p. 2025.01.22.634184.

70. H. S. Haraldsdóttir, I. Thiele, R. M. T. Fleming, Quantitative assignment of reaction directionality in a multicompartmental human metabolic reconstruction. *Biophys. J.* **102**, 1703–1711 (2012).

71. S. C. Burgess, F. M. H. Jeffrey, C. Storey, A. Milde, N. Hausler, M. E. Merritt, H. Mulder, C. Holm, A. D. Sherry, C. R. Malloy, Effect of murine strain on metabolic pathways of glucose production after brief or prolonged fasting. *Am. J. Physiol. Endocrinol. Metab.* **289**, E53-61 (2005).

72. S. Satapati, N. E. Sunny, B. Kucejova, X. Fu, T. T. He, A. Méndez-Lucas, J. M. Shelton, J. C. Perales, J. D. Browning, S. C. Burgess, Elevated TCA cycle function in the pathology of diet-induced hepatic insulin resistance and fatty liver. *J. Lipid Res.* **53**, 1080–1092 (2012).

73. C. M. Hasenour, M. L. Wall, D. E. Ridley, C. C. Hughey, F. D. James, D. H. Wasserman, J. D. Young, Mass spectrometry-based microassay of (2)H and (13)C plasma glucose labeling to quantify liver metabolic fluxes in vivo. *Am. J. Physiol. Endocrinol. Metab.* **309**, E191-203 (2015).

74. C. M. Hasenour, M. Rahim, J. D. Young, In vivo estimates of liver metabolic flux assessed by 13C-propionate and 13C-lactate are impacted by tracer recycling and equilibrium assumptions. *Cell Rep.* **32**, 107986 (2020).

75. Y. Wang, H. Kwon, X. Su, F. E. Wondisford, Glycerol not lactate is the major net carbon source for gluconeogenesis in mice during both short and prolonged fasting. *Molecular Metabolism* **31**, 36–44 (2020).

76. S. M. Turner, P. A. Linfoot, R. A. Neese, M. K. Hellerstein, Sources of plasma glucose and liver glycogen in fasted ob/ob mice. *Acta Diabetol.* **42**, 187–193 (2005).

77. J. B. S. Haldane, *Enzymes* (Longmans, Green and Co., London, England, 1930).

78. B. Cousins, Volume-and-Sampling - File Exchange - MATLAB CentralFile Exchange - MATLAB Central (2022). https://www.mathworks.com/matlabcentral/fileexchange/43596-volume-and-sampling.

79. S. Ohno, L.-E. Quek, J. R. Krycer, K. Yugi, A. Hirayama, S. Ikeda, F. Shoji, K. Suzuki, T. Soga, D. E. James, S. Kuroda, Kinetic trans-omic analysis reveals key regulatory mechanisms for insulin-regulated glucose metabolism in adipocytes. *iScience* **23**, 101479 (2020).

80. T. Lubitz, M. Schulz, E. Klipp, W. Liebermeister, Parameter balancing in kinetic models of cell metabolism. *J. Phys. Chem. B* **114**, 16298–16303 (2010).

81. UniProt Consortium, UniProt: The universal protein knowledgebase in 2023. *Nucleic Acids Res.* **51**, D523–D531 (2023).

82. Evan, Plot Groups of Stacked Bars - File Exchange - MATLAB CentralFile Exchange - MATLAB Central (2025). https://jp.mathworks.com/matlabcentral/fileexchange/32884-plot-groups-of-stacked-bars.

**Acknowledgments**

We thank our laboratory members for critically reading this manuscript. The computational analysis of this work was performed in part with support of the supercomputer system of the National Institute of Genetics (NIG), Research Organization of Information and Systems (ROIS). We used ChatGPT, DeepL, and Claude to assist in manuscript editing and coding.

**Funding**

This study was supported by the Japan Society for the Promotion of Science (JSPS) KAKENHI (Grant Numbers JP17H06300, JP17H06299, JP18H03979, JP21H04759, JP22K17992, JP23H04946, JP23H04939) (S.K.); the Japan Science and Technology Agency (JST) as part of CREST (JPMJCR2123, JPMJCR25T3) and as part of ASPIRE (JPMJAP24B1) (S.K.); The Uehara Memorial Foundation (S.K.); AMED Grant Number JP21zf0127001 (T.S.); JST, CREST Grant Number JPMJCR2123 (T.S.); MEXT KAKENHI Grant Number JP23H04946 (T.S.); World Premier International Research Center Initiative (WPI), Human Biology-Microbiome-Quantum Research Center (Bio2Q), MEXT, Japan (T.S.); JSPS KAKENHI JP24K11417 (A.H.); and the FOREST Program of the Japan Science and Technology Agency (JPMJFR2052) (A.H.).

**Author contributions**

Conceptualization: T.A., S.O., and S.K.

Methodology: T.A., S.O., A.H., and T.S.

Investigation: T.A., A.H., and T.S.

1015 Visualization: T.A.

1016 Funding acquisition: A.H., T.S., and S.K.

1017 Project administration: S.K.

1018 Supervision: S.K.

1019 Writing – original draft: T.A., S.O., and S.K.

1020 Writing – review & editing: T.A., S.O., A.H., T.S., and S.K.

1021

1022 **Competing interests**

1023 The authors declare no competing interests.

1024

1025 **Data and materials availability**

1026 The information on kinetic parameter (Michaelis-Menten constant and turnover number)
1027 distributions used for FCC calculation, the FCC values generated in this study, and the
1028 MATLAB code for GLEAM and the analysis of FCC and EC are deposited in GitHub
1029 (https://github.com/tabekawa/Thermodynamics_MouseLiver). All other data needed to
1030 evaluate the conclusions in the paper are present in the paper or the supplementary materials.

1031

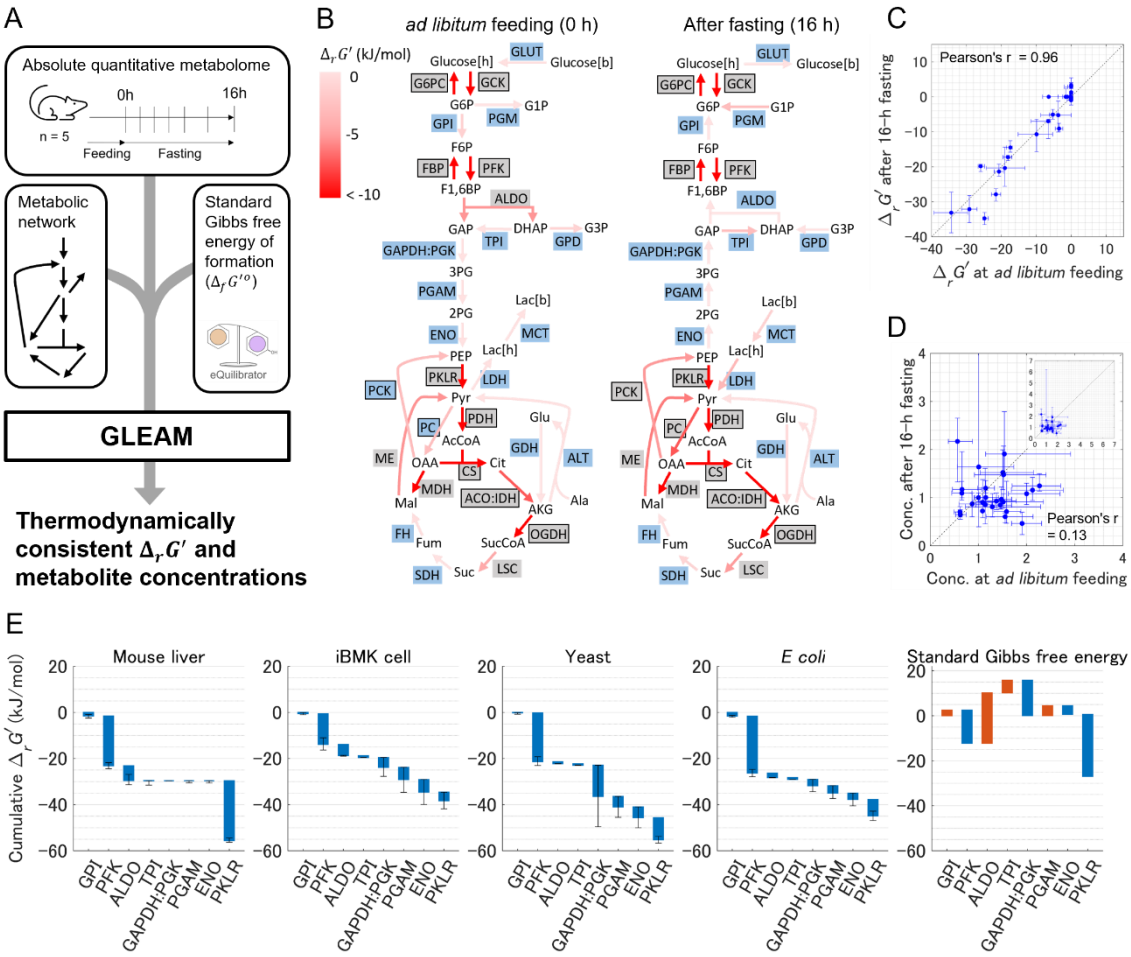


**Fig. 1: $\Delta_r G'$ landscape is robust against fasting despite metabolite concentration fluctuations.**

(**A**) Overview of the application of GLEAM to estimate $\Delta_r G'$ landscape in the mouse liver. Metabolomic data were acquired from the liver, skeletal muscle, and plasma of WT and *ob*/*ob* mice during fasting (data file S1) (*8*, *68*). $n$ = 5 biological replicates were used per group. The estimated metabolite concentrations, $\Delta_f G'^{\circ}$, and $\Delta_r G'$ values by GLEAM are shown in data file S2. (**B**) $\Delta_r G'$ landscape of glucose metabolism in mouse liver at *ad libitum* feeding and after 16-hour fasting. $\Delta_r G'$ is depicted by arrow colors. Shaded texts represent

1041 reaction names; boxed reactions are irreversible, while unboxed reactions are reversible. Blue
1042 shadings indicate near-equilibrium reactions with $\Delta_r G' > -5$ kJ/mol, and gray shadings
1043 indicate the other reactions with $\Delta_r G' \leq -5$ kJ/mol. Unshaded texts represent metabolites.
1044 [h], [m], and [b] indicate hepatic, myocytic, and blood metabolites, respectively.
1045 Abbreviations of reactions and metabolites are defined in the glossary and data file S3. (**C**)
1046 Comparison of $\Delta_r G'$ in WT mouse liver at *ad libitum* feeding and after 16-hour fasting. The
1047 forward direction ($\Delta_r G' < 0$) is defined as the reaction direction at *ad libitum* feeding.
1048 Pearson's correlation coefficient (r) is shown. Error bars show 95% confidence intervals. (**D**)
1049 Comparison of metabolite concentrations in WT mouse liver at *ad libitum* feeding and after
1050 16-hour fasting. Plotted metabolite concentrations represent those normalized by the mean
1051 value at all seven time points and two genotypes (14 conditions in total) to eliminate scale
1052 differences in concentrations among metabolites. Pearson's correlation coefficient (r) is
1053 shown. Error bars show 95% confidence intervals. Error bars show 95% confidence intervals.
1054 (**E**) Comparison of $\Delta_r G'$ in glycolysis across cell types and organisms. The data in iBMK
1055 cell, yeast, and *E. coli* were measured using LC-MS and isotope tracers (*26*). Standard Gibbs
1056 free energy was calculated by treating all metabolite concentrations as 1 M. The vertical axis
1057 represents cumulative $\Delta_r G'$ from GPI. Blue and orange bars depict negative and positive
1058 $\Delta_r G'$, respectively. Error bars show 95% confidence intervals.
1059
1060

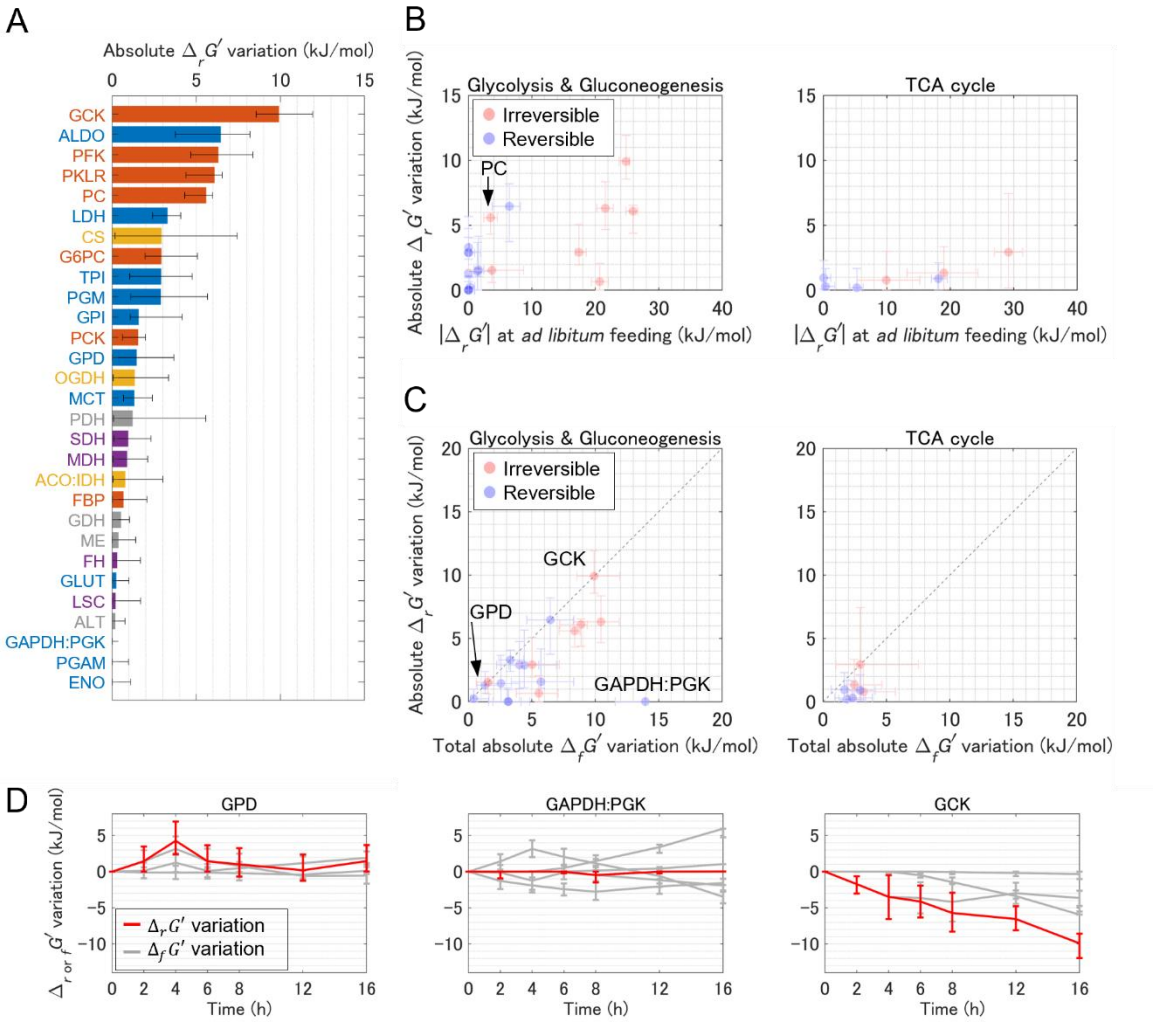


1061

1062 **Fig. 2: $\Delta_r G'$ maintenance during fasting is associated with metabolite concentration**

1063 **fluctuations in different ways among pathways.**

1064 (**A**) Absolute $\Delta_r G'$ variation = $|\Delta_r G'_{16\mathrm{h}} - \Delta_r G'_{0\mathrm{h}}|$. Bars depict irreversible reactions in

1065 glycolysis and gluconeogenesis (orange), reversible reactions in glycolysis and

1066 gluconeogenesis (blue), irreversible reactions in the TCA cycle (yellow), reversible reactions

1067 in the TCA cycle (purple), and the other reactions in the metabolic network (grey),

1068 respectively. Error bars show 95% confidence intervals. (**B**) Relationship between absolute

1069 $\Delta_r G'$ variation and reaction distance from equilibrium represented by absolute $\Delta_r G'$ at *ad*
1070 *libitum* feeding. Error bars show 95% confidence intervals. The reaction PC is highlighted
1071 and discussed in the Results section. (**C**) Comparison of absolute $\Delta_r G'$ variation of reactions
1072 and total absolute $\Delta_f G'$ variation of metabolites. Absolute $\Delta_f G'$ variation is dependent on
1073 concentrations of metabolites involved in the reaction, and defined by $\sum\left|S\left(\Delta_f G'_{16h} -\right.\right.$
1074 $\left.\left.\Delta_f G'_{0h}\right)\right|$. When $\Delta_f G'$ variation = $S\left(\Delta_f G'_{16h} - \Delta_f G'_{0h}\right)$ of the metabolites involved in the
1075 reaction are cancelled out, absolute $\Delta_r G'$ variation is smaller than total absolute $\Delta_f G'$
1076 variation, resulting in the reaction being plotted in the lower right. Plotted reactions for
1077 glycolysis and gluconeogenesis, and the TCA cycles are the same as Fig. 2B. Error bars show
1078 95% confidence intervals. The reactions GPD, GAPDH:PGK and GCK are highlighted and
1079 discussed in the Results section. (**D**) Time courses of $\Delta_r G'$ variation and $\Delta_f G'$ variation
1080 for representative reactions: GPD (small $\Delta_f G'$ variations), GAPDH:PGK (large $\Delta_f G'$
1081 variations which are canceled out), and GCK (large $\Delta_f G'$ variations which are not canceled
1082 out). Red and grey lines depict $\Delta_r G'$ variation and $\Delta_f G'$ variation, respectively. Error bars
1083 show 95% confidence intervals.
1084

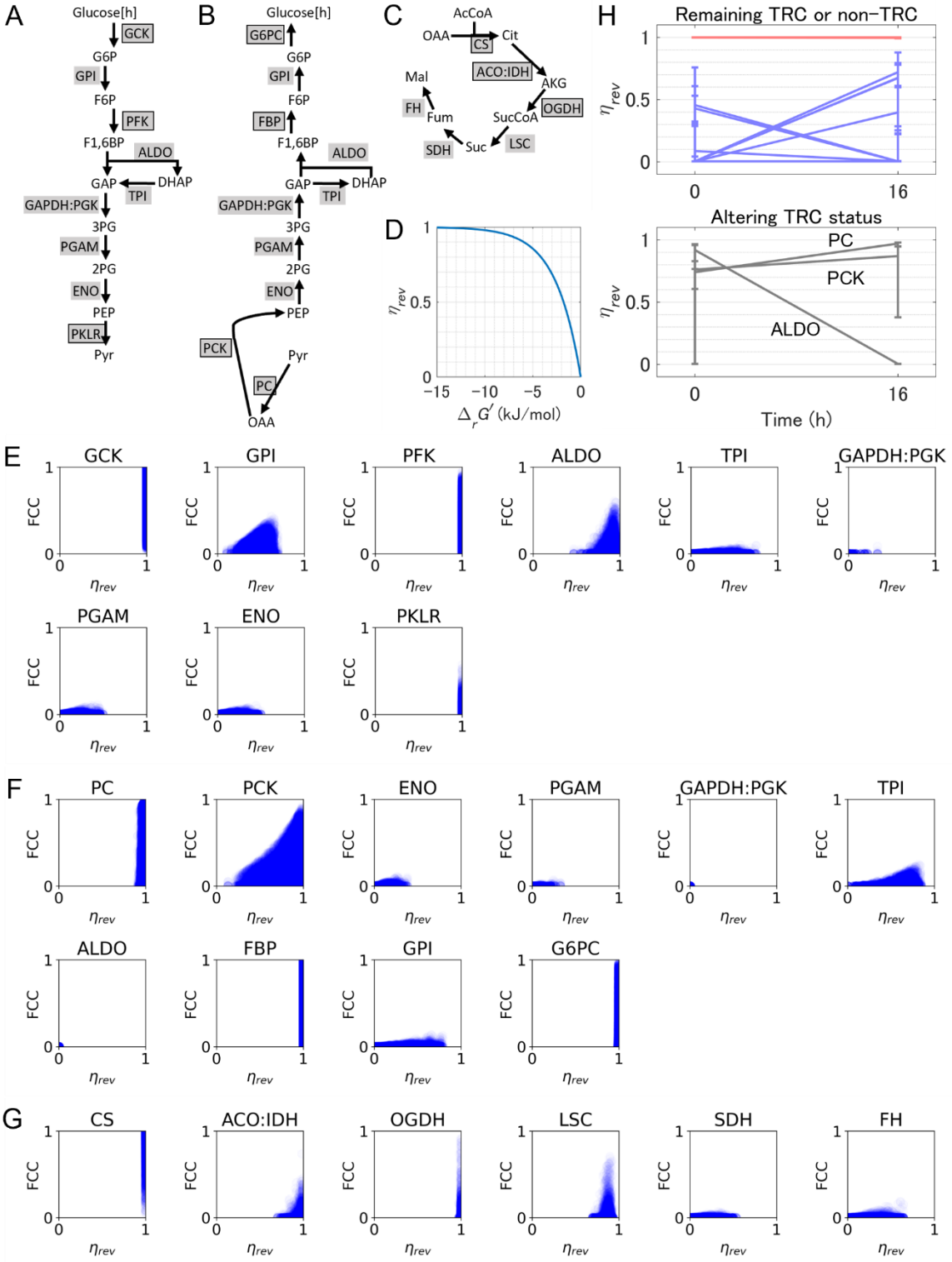
A
Glucose[h]
GCK
G6P
GPI
F6P
PFK
F1,6BP
ALDO
GAP
DHAP
TPI
GAPDH:PGK
3PG
PGAM
2PG
ENO
PEP
PKLR
Pyr
B
Glucose[h]
G6PC
G6P
GPI
F6P
FBP
F1,6BP
ALDO
GAP
DHAP
TPI
GAPDH:PGK
3PG
PGAM
2PG
ENO
PEP
PCK
Pyr
PC
OAA
C
AcCoA
OAA
CS
Cit
ACO:IDH
AKG
OGDH
SucCoA
LSC
Suc
SDH
Fum
FH
Mal
D
$\eta_{rev}$
$\Delta_r G'$ (kJ/mol)
H
Remaining TRC or non-TRC
Altering TRC status
PC
PCK
ALDO
Time (h)
E
GCK
GPI
PFK
ALDO
TPI
GAPDH:PGK
PGAM
ENO
PKLR
F
PC
PCK
ENO
PGAM
GAPDH:PGK
TPI
ALDO
FBP
GPI
G6PC
G
CS
ACO:IDH
OGDH
LSC
SDH
FH
FCC
$\eta_{rev}$

1085

1086 **Fig. 3: Thermodynamic Rate-limiting candidates (TRCs) were maintained during**
1087 **fasting.**
1088 (**A**) Glycolysis pathway where FCCs were calculated. (**B**) Gluconeogenesis pathway where
1089 FCCs were calculated. (**C**) The TCA cycle where FCCs were calculated. MDH was excluded
1090 from this TCA cycle because it proceeded in the opposite direction to the oxidative TCA
1091 cycle. (**D**) Correspondence between $\Delta_r G'$ and $\eta_{\mathrm{rev}}$. (**E-G**) Relationship between $\eta_{\mathrm{rev}}$ and
1092 FCC in glycolysis (**E**), gluconeogenesis (**F**), and the TCA cycle (**G**) in the mouse liver. $\eta_{\mathrm{rev}}$
1093 and FCC values of each point were calculated from each sampled set of metabolite
1094 concentrations and $\Delta_f G'^{\circ}$ values for the calculation of confidence intervals and sampled
1095 $K_{\mathrm{m}}$ values based on BRENDA database (see Methods). Metabolite concentrations at *ad*
1096 *libitum* feeding were used for glycolysis (**E**) and the TCA cycle (**G**), and those after 16-hour
1097 fasting were used for gluconeogenesis (**F**). Vertical variation is attributed to differences in
1098 $K_{\mathrm{m}}$ values and condition of the other reactions, while horizontal variation reflects differences
1099 in metabolite concentrations and $\Delta_f G'^{\circ}$. (**H**) Alterations of TRC status based on transitions
1100 in $\eta_{\mathrm{rev}}$ for reactions in glycolysis and gluconeogenesis before and after starvation. Red, blue,
1101 and grey lines depict reactions remaining TRC (5 reactions), reactions remaining non-TRC
1102 (10 reactions), and reactions altering their TRC status (either TRC or not) during fasting (3
1103 reactions), respectively. Error bars show 95% confidence intervals.
1104
1105

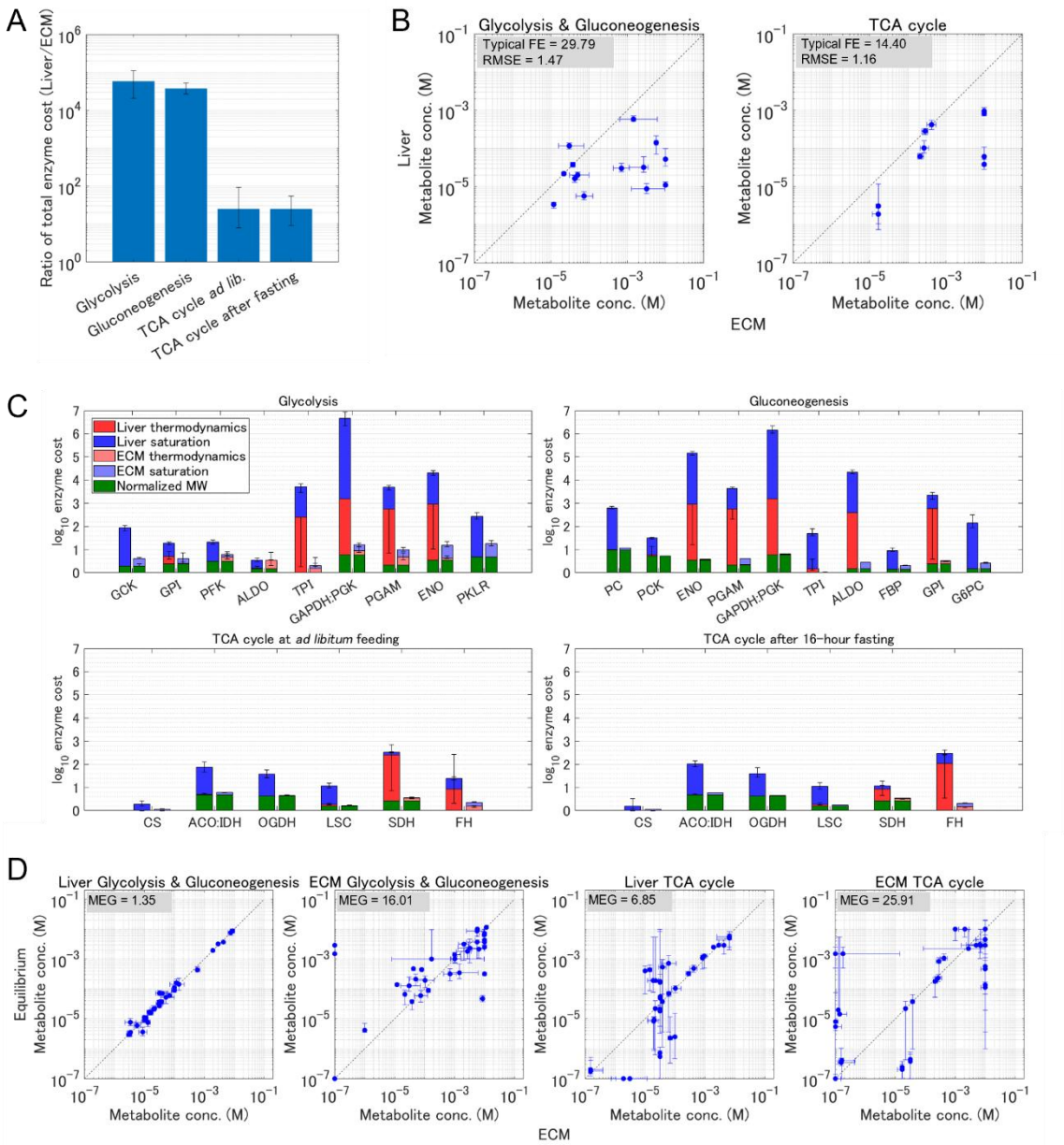


**Fig. 4: Glycolysis and gluconeogenesis achieve efficient switching by expending large enzyme costs.**

(**A**) Ratio of total enzyme cost under metabolite concentrations in the mouse liver and ECM (Liver/ECM). The total EC was calculated for glycolysis, gluconeogenesis, and the TCA

1111 cycle, which are the same as the pathways used for FCC calculation (Fig. 3A-C). Metabolite
1112 concentrations at *ad libitum* feeding and after 16-hour fasting were used for glycolysis and
1113 gluconeogenesis, respectively. $K_{\mathrm{m}}$ values for EC calculation were the geometric mean of
1114 data in the BRENDA database (data file S4). Error bars show 95% confidence intervals. EC
1115 in mouse liver, and metabolite concentrations and EC at ECM are shown in data file S4. (**B**)
1116 Comparison of metabolite concentrations in the mouse liver and ECM. Plotted data are for
1117 the measured metabolites, and the scatter plot for the TCA cycle includes the data both at *ad*
1118 *libitum* feeding and after 16-hour fasting. RMSE is the root mean square error on a $\log_{10}$-
1119 scale of ECM's prediction compared to metabolite concentrations in the mouse liver, and
1120 typical fold error (typical FE) = $10^{\mathrm{RMSE}}$. Error bars show 95% confidence intervals. Plotted
1121 data are for the measured metabolites. (**C**) EC of each reaction in glycolysis, gluconeogenesis,
1122 and the TCA cycle. The left and right bars of each reaction are EC in the mouse liver and
1123 ECM, respectively. Since the vertical axis represents a logarithmic scale, EC can be depicted
1124 by the stacked bar of normalized enzyme molecular weight (green), the effect of
1125 thermodynamics, $\eta_{\mathrm{rev}}^{-1}$ (red), and saturation, $\eta_{\mathrm{sat,s}}^{-1}$ (blue). Note that although the total
1126 Gibbs free energy change across the entire pathway in ECM is fixed to that in the mouse liver
1127 (see Methods), the sum of $\eta_{\mathrm{rev}}^{-1}$ differs due to the non-linear increase of $\eta_{\mathrm{rev}}$ over $\Delta_r G'$
1128 (Fig. 3D). Error bars show 95% confidence intervals. (**D**) Comparison of metabolite
1129 concentrations in the liver or ECM, and those for MEG calculation, where the reactions
1130 required to reverse for metabolic switching are at equilibrium. Plotted data are for the
1131 measured metabolites. Error bars show 95% confidence intervals. Metabolite concentrations

where the reactions required to reverse for metabolic switching are at equilibrium are shown in data file S5.

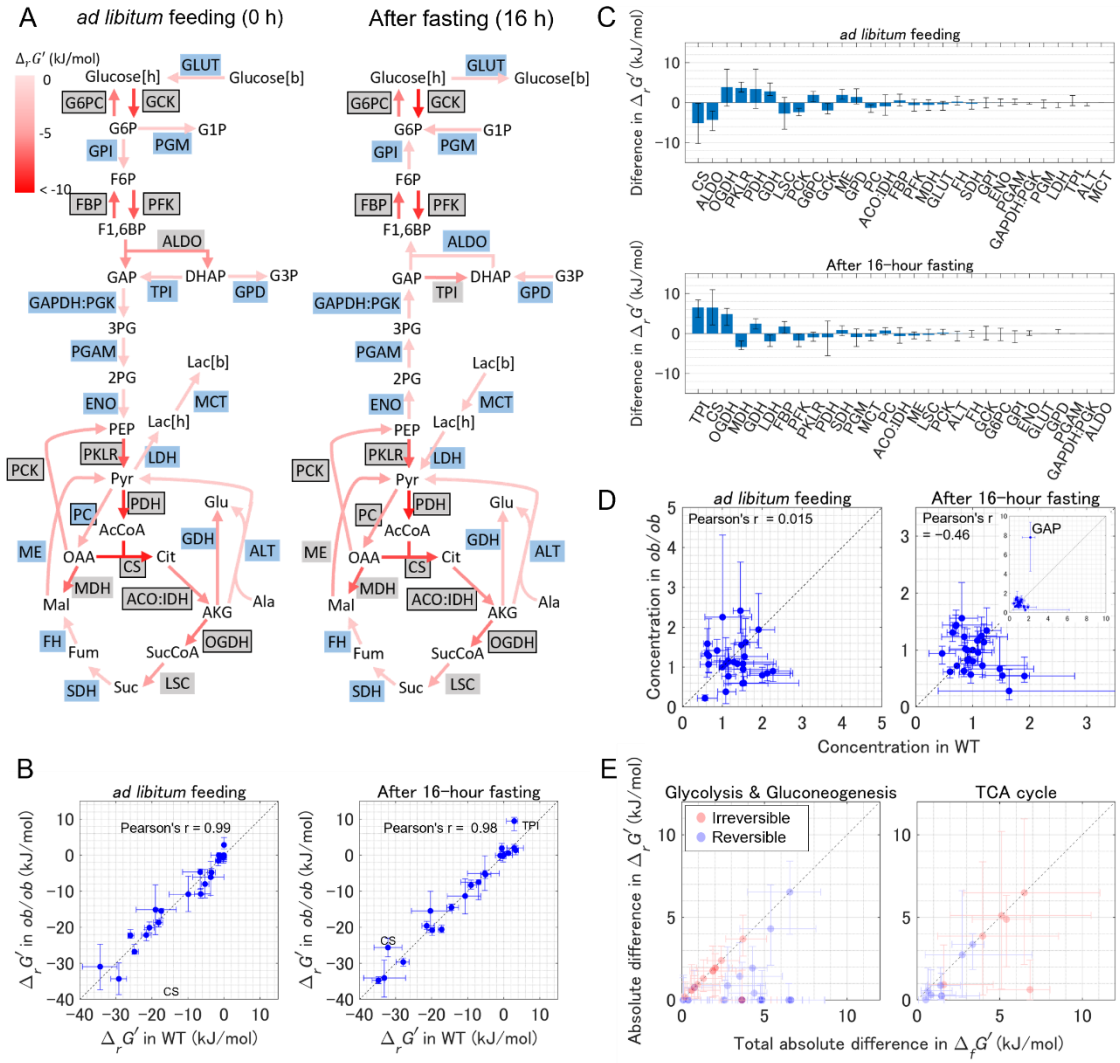


**Fig. 5: Robustness of $\Delta_r G'$ in the liver against obesity.**

(**A**) $\Delta_r G'$ landscape of glucose metabolism in *ob*/*ob* mouse liver at *ad libitum* feeding and after 16-hour fasting. $\Delta_r G'$ is depicted by arrow colors. Shaded texts represent reaction names; boxed reactions are irreversible, while unboxed reactions are reversible. Blue shadings indicate near-equilibrium reactions with $\Delta_r G' > -5$ kJ/mol, and gray shadings indicate the other reactions with $\Delta_r G' \leq -5$ kJ/mol. Unshaded texts represent metabolites.

1142 The estimated metabolite concentrations, $\Delta_f G'^{\circ}$, and $\Delta_r G'$ values by GLEAM are shown
1143 in data file S2. (**B**) Comparison of $\Delta_r G'$ in WT and *ob*/*ob* mouse liver. The forward direction
1144 ($\Delta_r G' < 0$) is defined as the reaction direction in WT at *ad libitum* feeding. Pearson's
1145 correlation coefficients (r) are shown. Error bars show 95% confidence intervals. (**C**)
1146 Difference in $\Delta_r G'$ between WT and *ob*/*ob* mouse liver ($\Delta_r G'_{ob/ob} - \Delta_r G'_{\mathrm{WT}}$). Reactions are
1147 arranged from left to right in order of decreasing absolute difference in $\Delta_r G'$. Error bars show
1148 95% confidence intervals. (**D**) Comparison of metabolite concentrations in WT and *ob*/*ob*
1149 mouse liver. Plotted data represent the concentrations normalized by the mean value at all
1150 seven time points and two genotypes *(i.e.*, 14 conditions) to eliminate scale differences in
1151 concentrations among metabolites. Pearson's correlation coefficients (r) are shown. Error
1152 bars show 95% confidence intervals. (**E**) Comparison of absolute difference in $\Delta_r G'$
1153 variation and total absolute deference in $\Delta_f G' = \sum\left|S\left(\Delta_f G'_{ob/ob} - \Delta_f G'_{\mathrm{WT}}\right)\right|$, between WT
1154 and *ob*/*ob* mouse liver. Plotted data includes those at *ad libitum* feeding and after 16-hour
1155 fasting. The reactions for glycolysis and gluconeogenesis, and the TCA cycles are the same
1156 as Fig. 2B. Error bars show 95% confidence intervals.
1157

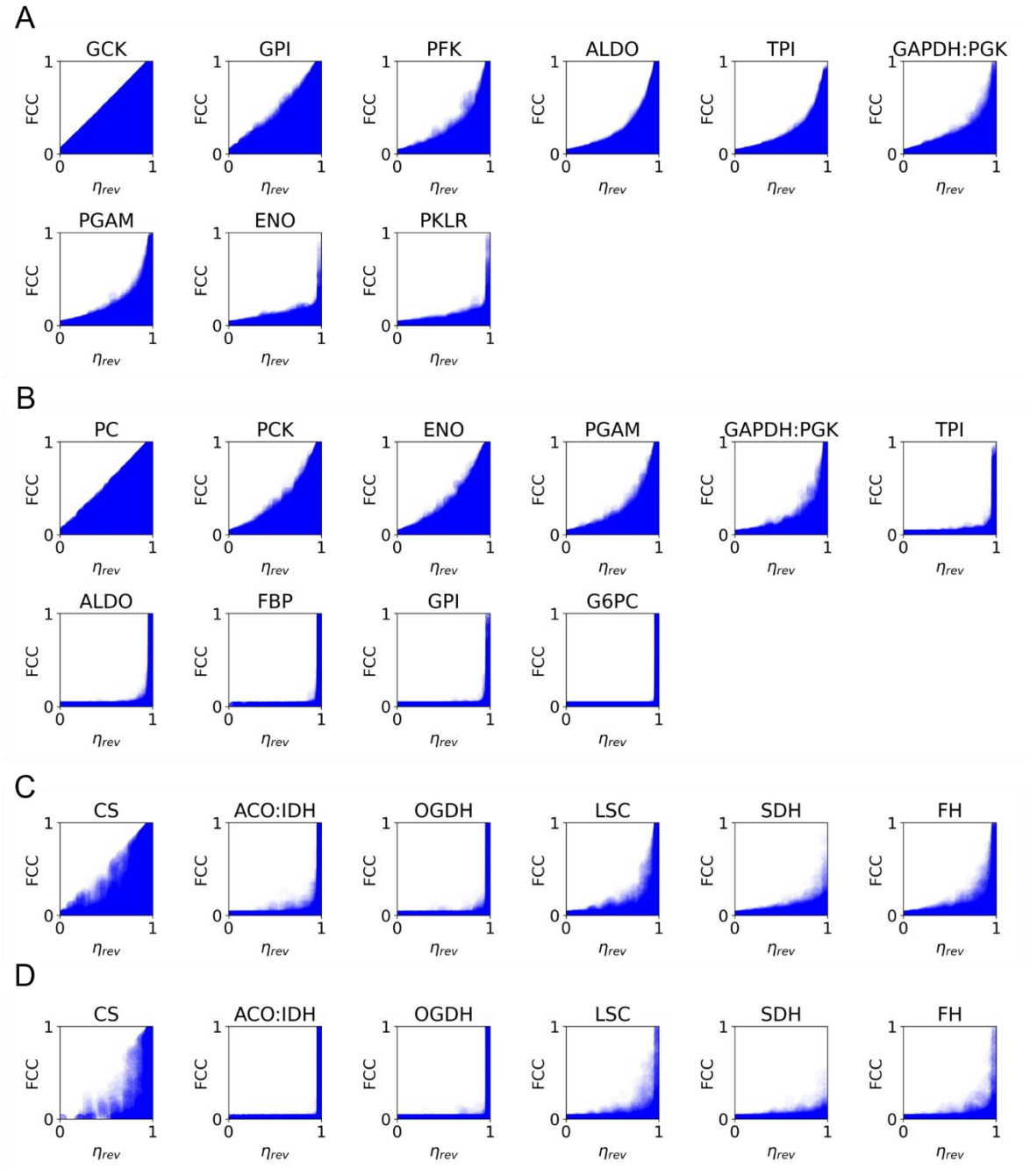


**Fig. S1: Relationship between $\eta_{\mathbf{rev}}$ and FCC for arbitrary $\Delta_r G'$ landscapes.** (**A-D**) Arbitrary $\Delta_r G'$ landscapes were generated by the uniform sampling of intrasellar metabolite concentrations under the blood metabolite concentrations at *ad libitum* feeding

1162 and after 16-hour fasting (see Methods). The arbitrary $\Delta_r G'$ landscapes at *ad libitum* feeding
1163 were used for FCC calculation in glycolysis (**A**) and the TCA cycle (**C**), while those after 16-
1164 hour fasting were used for gluconeogenesis (**B**), and the TCA cycle (**D**). Plotted data
1165 represents each sampled set of metabolite concentrations and $\Delta_f G'^{\circ}$, and $K_{\mathrm{m}}$ values.
1166

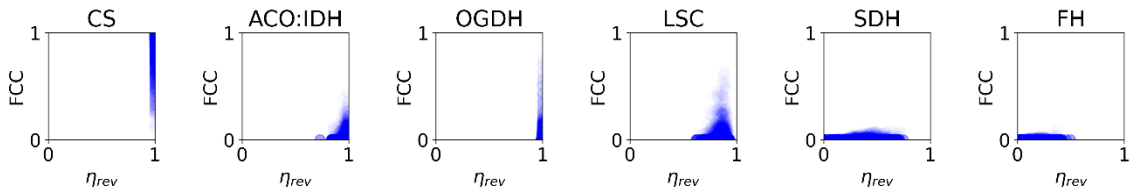


**Fig. S2: Relationship between $\eta_{\mathbf{rev}}$ and FCC in the TCA cycle in the mouse liver after 16-hour fasting.**

Plotted data represents each set of metabolite concentrations and $\Delta_f G'^{\circ}$ values sampled for the calculation of confidence intervals, and $K_{\mathrm{m}}$ values sampled based on BRENDA database (see Methods).

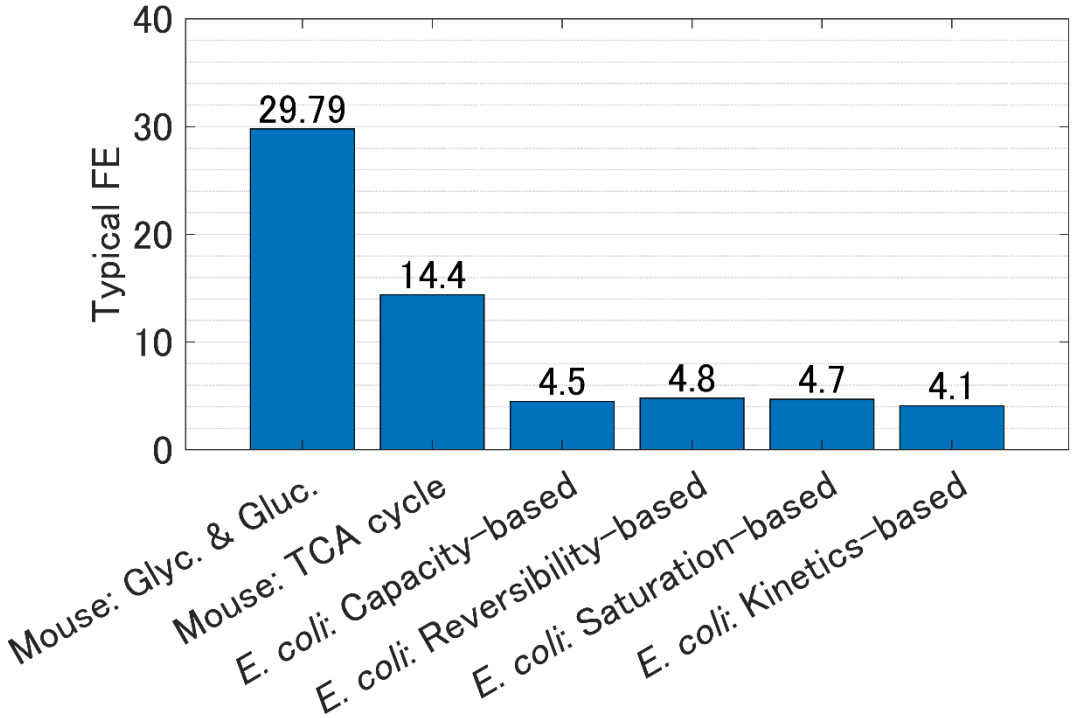


**Fig. S3: Typical fold error of ECM's prediction compared to metabolite concentrations in the mouse liver and *E. coli*.**

Glyc. and Gluc. means glycolysis and gluconeogenesis, respectively. Minimizations of total EC in *E. coli* were conducted for the metabolic network, which consists of glycolysis, the pentose phosphate pathway, and the TCA cycle, assuming four different enzymatic rate equations (see Methods).

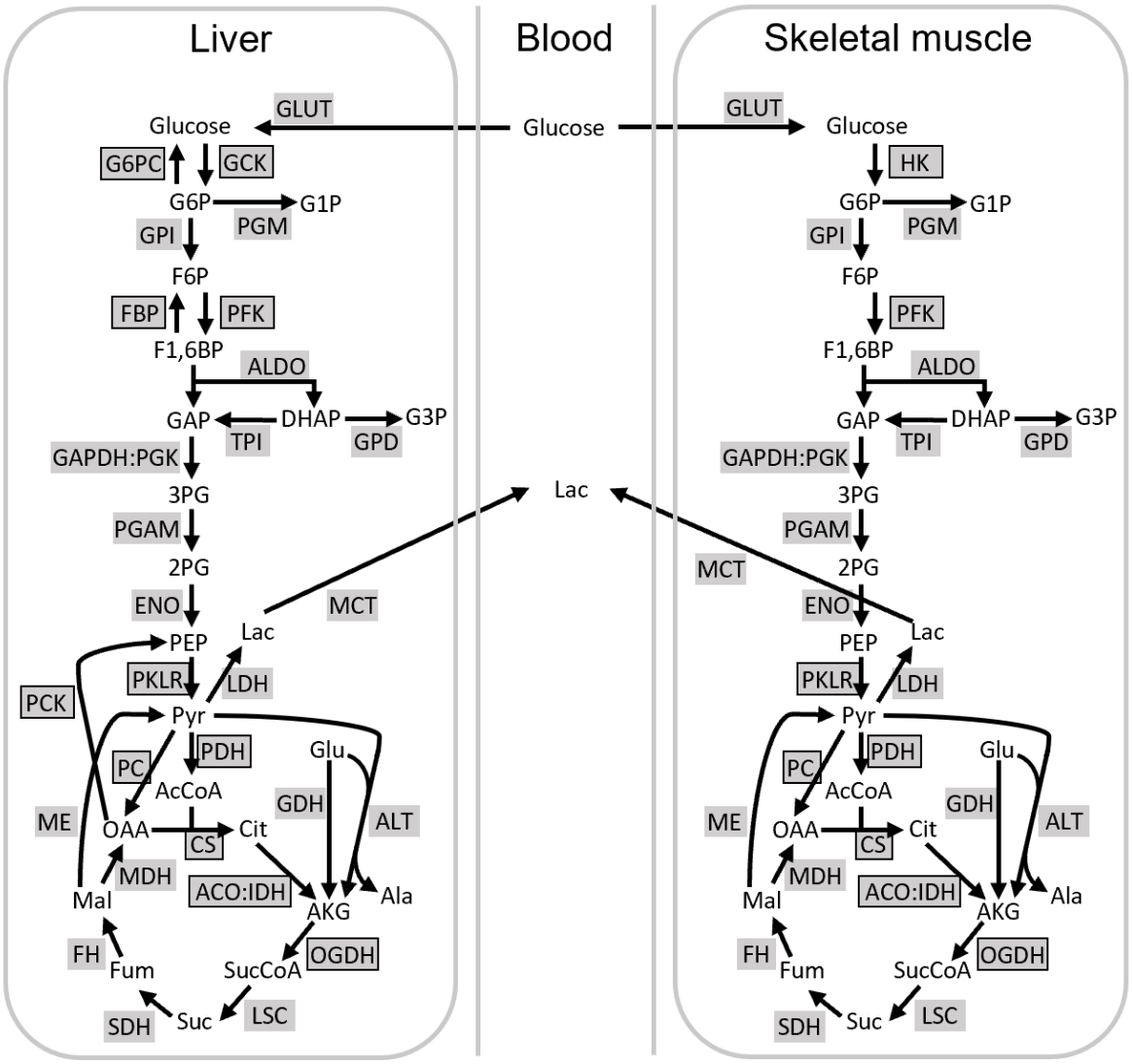


**Fig. S4: A whole metabolic network used to estimate $\Delta_r G'$ landscape.**

Shaded texts represent reaction names; boxed reactions are irreversible, while unboxed reactions are reversible. Unshaded texts represent metabolites. Although the network consists of liver, blood, and skeletal muscle to improve the accuracy of $\Delta_f G'^{\circ}$ estimation, only the $\Delta_r G'$ landscape of reactions and transporters in the liver were discussed in this study because the concentration of unmeasured major metabolites, such as glucose in skeletal muscle, cannot be estimated with sufficient accuracy due to a lack of reactions.

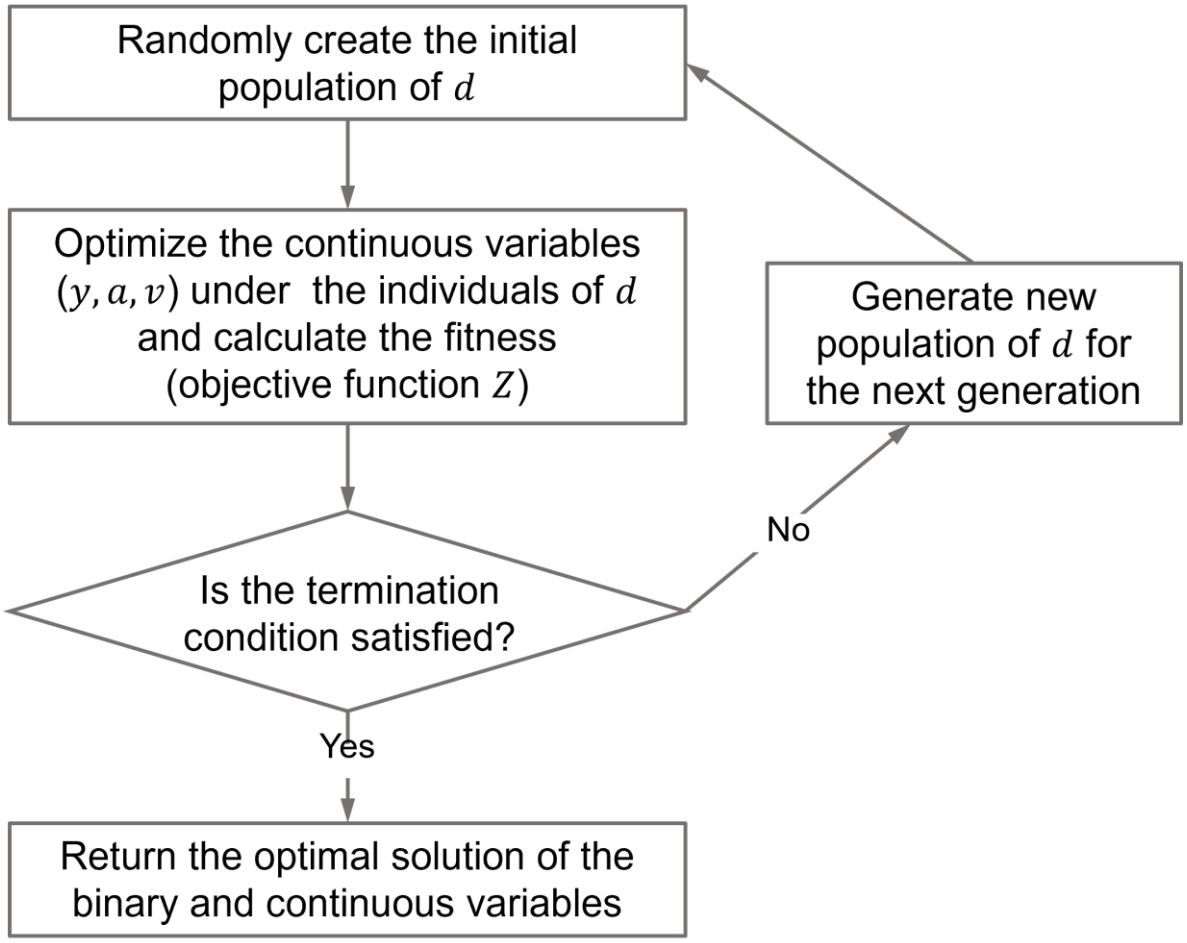


**Fig. S5: Flowchart of the bilevel optimization problem in GLEAM.**

The optimization problems for the continuous and binary variables are treated as the lower-level and upper-level problems, respectively. The optimal solution of GLEAM was selected after solving this bilevel optimization 10 times.

1196 **Supplementary tables**

1197 **Table S1: Upper and lower bounds of metabolite concentrations and cofactor ratios.**

| Metabolites, cofacer ratios | Lower bounds | Upper bounds | References |
|---|---|---|---|
| Intracellular glucose*1 | $1.0\times10^{-3}$ M | $1.5\times10^{-2}$ M | (*81*) |
| Hepatic Pi | $3.0\times10^{-3}$ M | $4.3\times10^{-3}$ M | (*82*) |
| Myocytic Pi | $3.0\times10^{-3}$ M | $9.0\times10^{-3}$ M | (*82*, *83*) |
| $CO_2$, $HCO_3^-$ | $1.5\times10^{-3}$ M | $2.5\times10^{-3}$ M | (*84*) |
| $NH_3$ | $2.0\times10^{-4}$ M | $1.0\times10^{-3}$ M | (*85*) |
| Other intracellular metabolites*1 | $1.0\times10^{-7}$ M | $1.0\times10^{-2}$ M | (*26*) |
| Blood metabolites | $1.0\times10^{-7}$ M | $1.0\times10^{-1}$ M | (*86*) |
| ATP/ADP | 1 | 10 | (*83*, *87*, *88*) |
| $NAD^+$/NADH | 3 | 10 | (*89*) |
| GTP/GDP | 1 | 10 | (*90*) |
| $NADP^+$/NADPH | 0.05 | 0.2 | (*91*) |

1198 *1: The upper bounds of intracellular glucose, G6P, F6P, F1,6BP, DHAP, GAP, 3PG, 2PG,

1199 PEP, G1P, G3P, and Lac in *ob*/*ob* mouse are $1.0\times10^{-1}$ M.

1200

1201 **Table S2: Metabolite concentrations and a cofactor ratio involved in PKLR between**

1202 **mouse liver and other cell types.**

| Metabolites, cofacer ratios | Mouse liver | iBMK cell | Yeast | *E. coli* |
|---|---|---|---|---|
| PEP | $2.02\times10^{-5}$ M | $1.16\times10^{-5}$ M | $2.91\times10^{-5}$ M | $1.84\times10^{-4}$ M |
| Pyr | $3.77\times10^{-5}$ M | $5.88\times10^{-3}$ M | $9.40\times10^{-3}$ M | $3.66\times10^{-3}$ M |
| ATP/ADP | 1.00 | 8.21 | 3.95 | 17.35 |

1203 Metabolite concentrations in iBMK cell, Yeast, and E. coli were measured by LC-MS (*86*).

1204

1205 **Supplementary data file legends**

1206 **Data File S1: Metabolomic and $\Delta_f G'^\circ$ data used as input for GLEAM.**

1207 This file includes the input metabolomic and $\Delta_f G'^\circ$ data for GLEAM (logarithmic mean of
1208 metabolome concentrations, $\Delta_f G'^\circ$ values, and variance-covariance matrix of metabolite
1209 concentrations and $\Delta_f G'^\circ$s). The metabolite concentrations were measured form from WT
1210 and *ob*/*ob* mice in previous studies (*8*, *69*), and $\Delta_f G'^\circ$ data were retrieved from eQuilibrator
1211 database (*53*). NaN represents unmeasured metabolite. [h], [m], and [b] indicate hepatic,
1212 myocytic, and blood compartment, respectively. The logarithmic mean of metabolite
1213 concentrations shown in this file is converted from a logarithmic scale to a linear scale.

1214

1215 **Data File S2: Thermodynamically consistent metabolite concentrations, $\Delta_f G'^\circ$, and**
1216 **$\Delta_r G'$ estimated by GLEAM.**

1217 This file includes the thermodynamically consistent metabolite concentrations, $\Delta_f G'^\circ$, and
1218 $\Delta_r G'$ values in mouse liver and blood estimated by GLEAM. For glucose and lactate, hepatic
1219 and blood metabolites are distinguished by the [h] and [b], respectively.

1220

1221 **Data File S3: Metabolites and reactions in the metabolic network for glucose**
1222 **metabolism in mice.**

1223 This file includes definitions of metabolite abbreviations, reaction abbreviations, and the
1224 metabolic network *i.e.* the stoichiometric matrix for glucose metabolism used in this study.

1225 In the Reactions and Stoichiometric matrix sheet, [h], [m], and [b] indicate hepatic, myocytic,
1226 and blood compartments, respectively.
1227
1228 **Data File S4: EC calculation in mouse liver and ECM.**
1229 This file includes EC values within glycolysis, gluconeogenesis, and the TCA cycle in mouse
1230 liver and EC, metabolite concentrations in ECM, and geometric mean of Michaelis-Menten
1231 constant retrieved from BRENDA database (*51*) used for EC calculation. In EC calculation,
1232 metabolite concentrations at *ad libitum* feeding were used for glycolysis and the TCA cycle,
1233 and those after 16-hour fasting were used for gluconeogenesis and the TCA cycle. EC is
1234 product of normalized molecular weight, $1/\eta_{\mathrm{rev}}$, and $1/\eta_{\mathrm{sat,s}}$.
1235
1236 **Data File S5: Metabolite concentrations where the reactions required to reverse for**
1237 **metabolic switching are at equilibrium, as determined by MEG calculation.**
1238 This file includes the metabolite concentrations that are the optimal solution to the
1239 optimization problem in MEG calculation for glycolysis, gluconeogenesis, and the TCA
1240 cycle. At these concentrations, the reactions required to reverse for directional switching of
1241 the pathways are at equilibrium with the minimum concentration changes from mouse liver
1242 or ECM.
1243

1244 **Supplementary references**

1245 81. P. A. Wals, J. Katz, A concentration gradient of glucose from liver to plasma.
1246 *Metabolism* **42**, 1492–1496 (1993).

1247 82. U. Till, D. Brox, H. Frunder, "Orthophosphate Turnover in the Extracellular and
1248 Intracellular Space of Mouse Liver" (1969);
1249 https://febs.onlinelibrary.wiley.com/doi/full/10.1111/j.1432-1033.1969.tb00806.x.

1250 83. R. L. Veech, J. W. Lawson, N. W. Cornell, H. A. Krebs, Cytosolic phosphorylation
1251 potential. *J. Biol. Chem.* **254**, 6538–6547 (1979).

1252 84. D. A. Beard, H. Qian, Thermodynamic-based computational profiling of cellular
1253 regulatory control in hepatocyte metabolism. *American Journal of Physiology-*
1254 *Endocrinology and Metabolism* **288**, E633–E644 (2005).

1255 85. A. J. Meijer, W. H. Lamers, R. A. Chamuleau, Nitrogen metabolism and ornithine cycle
1256 function. *Physiol. Rev.* **70**, 701–748 (1990).

1257 86. H. Ando, K. Ushijima, S. Shimba, A. Fujimura, Daily Fasting Blood Glucose Rhythm
1258 in Male Mice: A Role of the Circadian Clock in the Liver. *Endocrinology* **157**, 463–469
1259 (2016).

1260 87. S. Mörikofer-Zwez, P. Walter, Binding of ADP to rat liver cytosolic proteins and its
1261 influence on the ratio of free ATP/free ADP. *Biochem. J* **259**, 117–124 (1989).

1262 88. T. W. Traut, Physiological concentrations of purines and pyrimidines. *Mol. Cell.*
1263 *Biochem.* **140**, 1–22 (1994).

1264 89. S.-J. Lin, L. Guarente, Nicotinamide adenine dinucleotide, a metabolic regulator of
1265 transcription, longevity and disease. *Curr. Opin. Cell Biol.* **15**, 241–246 (2003).

1266 90. J. L. Bos, H. Rehmann, A. Wittinghofer, GEFs and GAPs: Critical Elements in the
1267 Control of Small G Proteins. *Cell* **129**, 865–877 (2007).

1268 91. R. L. Veech, L. V. Eggleston, H. A. Krebs, The redox state of free nicotinamide–adenine
1269 dinucleotide phosphate in the cytoplasm of rat liver. *Biochem. J* **115**, 609–619 (1969).